



# MIT Open Access Articles



## *Constraints on the Distances and Timescales of Solid Migration in the Early Solar System from Meteorite Magnetism*

The MIT Faculty has made this article openly available. **Please share** how this access benefits you. Your story matters.

<b>As Published</b>	10.3847/1538-4357/AB91AB
<b>Publisher</b>	American Astronomical Society
<b>Version</b>	Final published version
<b>Citable link</b>	<a href="https://hdl.handle.net/1721.1/133939">https://hdl.handle.net/1721.1/133939</a>
<b>Terms of Use</b>	Article is made available in accordance with the publisher's policy and may be subject to US copyright law. Please refer to the publisher's site for terms of use.



# Constraints on the Distances and Timescales of Solid Migration in the Early Solar System from Meteorite Magnetism

James F. J. Bryson<sup>1,2,3</sup> , Benjamin P. Weiss<sup>2</sup>, John B. Biersteker<sup>2</sup> , Ashley J. King<sup>4</sup>, and Sara S. Russell<sup>5</sup>

<sup>1</sup>Department of Earth Sciences, University of Cambridge, Downing Street, Cambridge CB2 3EQ, UK; [jfjb2@cam.ac.uk](mailto:jfjb2@cam.ac.uk)

<sup>2</sup>Department of Earth, Atmospheric, and Planetary Sciences, Massachusetts Institute of Technology, 77 Massachusetts Avenue, Cambridge, MA 02139, USA

<sup>3</sup>Department of Earth Sciences, University of Oxford, South Parks Road, Oxford OX1 3AN, UK

<sup>4</sup>Planetary and Space Sciences, Department of Physical Sciences, Open University, Milton Keynes MK7 6AA, UK

<sup>5</sup>Department of Earth Sciences, Natural History Museum, Cromwell Road, London SW7 5BD, UK

Received 2020 January 31; revised 2020 May 6; accepted 2020 May 7; published 2020 June 17

## Abstract

The migrations of solid objects throughout the solar system are thought to have played key roles in disk evolution and planet formation. However, our understanding of these migrations is limited by a lack of quantitative constraints on their timings and distances recovered from laboratory measurements of meteorites. The protoplanetary disk supported a magnetic field that decreased in intensity with heliocentric distance. As such, the formation distances of the parent asteroids of ancient meteorites can potentially be constrained by paleointensity measurements of these samples. Here, we find that the WIS 91600 ungrouped C2 chondrite experienced an ancient field intensity of  $4.4 \pm 2.8 \mu\text{T}$ . Combined with the thermal history of this meteorite, magnetohydrodynamical models suggest the disk field reached  $4.4 \mu\text{T}$  at  $\sim 9.8$  au, indicating that the WIS 91600 parent body formed in the distal solar system. Because WIS 91600 likely came to Earth from the asteroid belt, our recovered formation distance argues that this body previously traveled from  $\sim 10$  au to 2–3 au, supporting the migration of asteroid-sized bodies throughout the solar system. WIS 91600 also contains chondrules, calcium-aluminum-rich inclusions and amoeboid olivine aggregates, indicating that some primitive millimeter-sized solids that formed in the innermost solar system migrated outward to  $\sim 10$  au within  $\sim 3$ –4 Myr of solar system formation. Moreover, the oxygen isotopic compositions of proposed distal meteorites (WIS 91600, Tagish Lake and CI chondrites) argue that the CM, CO, and CR chondrites contain micrometer-scale dust and ice that originated in the distal solar system.

*Unified Astronomy Thesaurus concepts:* Meteorites (1038); Magnetic fields (994); Primordial magnetic fields (1294); Asteroid belt (70); Kuiper belt (893); Protoplanetary disks (1300); Chondrules (229); Chondrites (228)

## 1. Introduction

A broad range of solid objects have been proposed to have migrated throughout the early solar system. These objects include micrometer-scale dust and ice particles (Scott 2007), ancient millimeter-sized solids such as chondrules and calcium-aluminum-rich inclusions (CAIs; the oldest objects that formed in the solar system; Ciesla 2007), 1–1000 km sized planetesimals (Raymond & Izidoro 2017), and the terrestrial planets and gas giants (Gomes et al. 2005; Walsh et al. 2011; DeMeo & Carry 2014). All of these objects are predicted to have migrated within the first  $\sim 4$ –5 million years (Myr) after CAI formation when a protoplanetary disk of dust and gas existed in the solar system. The orbital parameters of some Kuiper Belt objects indicate that giant planet and planetesimal migration continued for hundreds of millions of years after this early period (Nesvorny 2018).

The migrations of these solids have been proposed to have played key roles in forming the terrestrial planets (Walsh et al. 2011), establishing the bulk compositions of these bodies (Gomes et al. 2005), populating the asteroid belt (Raymond & Izidoro 2017), and generating the present-day architecture of the solar system (DeMeo & Carry 2014). Despite their potential importance, the insight that has previously been recovered from the meteorite record into these migrations is largely qualitative, limiting our understanding of these key processes. For example, the measured isotopic compositions of carbonaceous chondrites argue that the parent asteroids of these meteorites originally formed beyond the orbit of Jupiter (Kruijjer et al. 2017).

However, these meteorites have been observed to be coming to Earth from the asteroid belt (i.e., within the orbit of Jupiter; Granvik & Brown 2018). Together, these observations support the inward migration of some asteroid-sized bodies, but do not provide quantitative constraints on the distances and timings involved in this process. Moreover, fragments of CAIs have been found in the material collected from the coma of comet 81P/Wild2 during the Stardust mission (Brownlee et al. 2006; Joswiak et al. 2017), which, coupled with their inferred origin in the innermost solar system ( $\lesssim 1$  au), argues that these objects migrated throughout the protoplanetary disk. However, data collected from these fragments have struggled to constrain the timings and distances involved in this motion, limiting our understanding of its driving mechanism and the processes by which some millimeter-sized solids were able to survive the early solar system (Cuzzi et al. 2003).

These limits on our understanding of solid migration stem partly from difficulties in recovering numerical constraints on the formation distances and orbital evolutions of individual meteorite components and parent bodies from laboratory measurements of these samples. Recently, paleomagnetic measurements of ancient meteorites and their components have been proposed as a method of constraining the formation distances of these objects (Bryson et al. 2020). Theory has long suggested that our protoplanetary disk supported a magnetic field (Wardle 2007). Recent paleomagnetic measurements of individual chondrules (Fu et al. 2014, 2020) and whole meteorites (Cournede et al. 2015; Bryson et al. 2019a) as well

as spacecraft observations of comet 67P/Churyumov–Gerasimenko (Biersteker et al. 2019) have provided experimental evidence supporting the existence of such a field within our disk. Paleomagnetic measurements and petrographic observations of individual chondrules from the CR chondrites (Schrader et al. 2018; Fu et al. 2020) argue that the disk likely persisted until at least  $\sim 3.7$  Myr after CAI formation. Similar measurements and observations of the volcanic angrites (Wang et al. 2017) and CH chondrites (Morris et al. 2015) argue that the disk then dissipated sometime between  $\sim 3.8$  and 4.8 Myr after CAI formation. Magnetohydrodynamical (MHD) models of the disk (Bai & Goodman 2009; Bai 2015) and paleomagnetic measurements of meteorites (Fu et al. 2014; Cournede et al. 2015; Bryson et al. 2019a) suggest that this field consisted of two components: an instantaneous component that changed orientation on a period of possibly  $\sim 100$ – $1000$  yr (Bai & Goodman 2009), and a time-averaged component that could have been directionally stable over the lifetime of the disk (Bai 2015). These models and measurements also indicate that the mean intensity of both components of this field likely decreased by greater than two orders of magnitude with increasing distance from the Sun over  $\sim 30$  au. As such, the paleointensities recovered from bulk meteorites and their components that recorded magnetic remanences within the lifetime of the solar nebula can be used as a proxy for the formation distances of their parent asteroids within the solar system.

This approach has been applied to the ungrouped C2 chondrite Tagish Lake, a unique meteorite with mineralogical and chemical signatures (Brown et al. 2000; Hiroi et al. 2001; Grady et al. 2002; Zolensky et al. 2002; Fujiya et al. 2019) that suggest its parent body formed at a larger heliocentric distance than those of most other meteorites (i.e.,  $\gtrsim 4$  au; Desch et al. 2018). Tagish Lake was extensively aqueously altered on its parent asteroid (Zolensky et al. 2002). One of the secondary phases that formed during this process was magnetite, which acquired a chemical remanent magnetization (CRM) of the magnetic fields experienced by this meteorite as this phase precipitated. The magnetite in Tagish Lake likely formed sometime between  $\sim 3$  and 4 Myr after CAI formation (Zolensky et al. 2002; Fujiya et al. 2013; Bryson et al. 2020) and the whole process of aqueous alteration likely lasted  $\sim 0.1$ – $1$  Myr (Krot et al. 2006). As such, this magnetite is expected to have acquired a CRM of the time-averaged stable component of the nebula field. The paleointensity recovered from Tagish Lake is very weak ( $< 0.15 \mu\text{T}$ ; Bryson et al. 2020), which, combined with magnetohydrodynamical models of the stable component of the nebula field (Bai 2015), suggests the Tagish Lake parent body likely formed in the far reaches of the solar system ( $\gtrsim 8$ – $13$  au) at a significantly larger heliocentric distance than most other meteorite parent bodies have been proposed to have formed.

The relatively weak intensity of the stable component of the nebula field at large heliocentric distances means that the paleomagnetic measurements of Tagish Lake were only able to recover a limit on the paleointensity experienced by this meteorite ( $< 0.15 \mu\text{T}$ ), which is only capable of constraining the formation distance of its parent body to a range of values ( $\gtrsim 8$ – $13$  au). Furthermore, paleointensity recovery from CRMs is relatively poorly constrained compared to thermoremanent magnetizations (TRMs) acquired when magnetic grains cool in the presence of a field, introducing an uncertainty on the

paleointensity recovered from Tagish Lake (up to a factor of five; McClelland 1996). Finally, Tagish Lake could only be successfully demagnetized using alternating fields (AF) rather than heating (due to chemical alteration during heating), meaning that paleointensities could only be recovered from anhysteretic remanent magnetization (ARM) and isothermal remanent magnetization (IRM) methods. Although these paleointensities can be converted to thermal-equivalent values, uncertainties in the factors required for these conversions introduce an additional uncertainty on the paleointensity recovered from Tagish Lake (which is also up to a factor of five; Weiss et al. 2010; Weiss & Tikoo 2014).

These limits and uncertainties could be overcome by measuring the natural remanent magnetization (NRM) carried by a meteorite that underwent mild heating and quick cooling within the lifetime of the nebula. A handful of CM (Mighei-like), CI-like (Ivuna-like), and C2 (ungrouped aqueously altered carbonaceous) chondrites display compositional, mineralogical, and textural evidence that they underwent brief and mild heating on their parent asteroids likely following an impact (Nakamura 2005). Such a heated meteorite would have recorded a partial TRM (pTRM) as it cooled. As such, the uncertainties associated with recovering paleointensities from a CRM would not apply to this meteorite. Moreover, if the remanence carried by this meteorite could be thermally demagnetized without significant chemical alteration, the paleointensity recovered from this sample would not suffer from the uncertainties associated with converting ARM or IRM paleointensities to thermal-equivalent values. Additionally, the quick cooling of this meteorite means its pTRM will have been imparted by the instantaneous component of the nebula field. This component was potentially approximately an order of magnitude more intense than the stable component (Bai & Goodman 2009; Bai 2015), meaning a precise paleointensity could possibly be recovered from this meteorite rather than a limit on this value. The paleointensity recovered from such a meteorite could, therefore, provide a relatively well-constrained estimate of the formation distance of its parent body. Utilizing this approach on a meteorite that also potentially originates from the far reaches of our solar system could provide much-needed support to the claim that some meteorites originate from this region of the solar system, as well as a more accurate estimate of the heliocentric distances at which the parent bodies of such meteorites could have formed.

With this goal in mind, we conducted a paleointensity experiment on the Wisconsin Range (WIS) 91600 meteorite. WIS 91600 is a low shock (S1), very weakly weathered (W1 or A/B) ungrouped C2 chondrite (Rubin et al. 2007; Choe et al. 2010) that was extensively aqueously altered when it was part of the regolith of its parent body (Yabuta et al. 2010). WIS 91600 displays close similarities to Tagish Lake in its reflectance spectra (Hiroi et al. 2005), oxygen isotopic composition (Choe et al. 2010), mineralogy (Tonui et al. 2014), conditions of aqueous alteration and insoluble organic matter (IOM) content (Yabuta et al. 2010), as well as broad similarities to the CM and CI chondrites in its texture, chemistry, and petrology (Birjukov & Ulyanov 1996; Rubin et al. 2007; Moriarty et al. 2009; Braukmuller et al. 2018). The similar nature (Yabuta et al. 2010; Tonui et al. 2014), timing (Fujiya et al. 2012, 2013), and extent (Rubin et al. 2007; Howard et al. 2015) of aqueous alteration in WIS 91600, Tagish Lake, the CM chondrites and the CI chondrites suggest that the parent bodies of all of these meteorites likely accreted

sometime between  $\sim 3$  and 4 Myr after CAI formation (Doyle et al. 2015). Magnetite and pyrrhotite were generated in all of these meteorites as they underwent aqueous alteration shortly after their parent body accreted (likely within  $\sim 0.5$  Myr; Zolensky et al. 2002; Tonui et al. 2014; Pravdivtseva et al. 2018). Similarly to Tagish Lake (Bryson et al. 2020) and the CM chondrites (Cournede et al. 2015), we therefore expect that WIS 91600 initially recorded a CRM of the stable component of our nebula field during this process. However, WIS 91600 displays mineralogical and chemical evidence that it was briefly heated to between 400 and 500°C on its parent body after or near the end of the main phase of aqueous alteration (Moriarty et al. 2009; Yabuta et al. 2010; Garenne et al. 2014; Tonui et al. 2014; Quirico et al. 2018). Hence, magnetic grains in this meteorite with blocking temperatures below its peak metamorphic temperature are expected to carry a pTRM overprint of any fields it experienced as it cooled following this heating. The remanence carried by grains with blocking temperatures greater than this peak temperature is still expected to be the CRM of the stable component of the nebula field.

The thermal and aqueous history of WIS 91600, therefore, mean this meteorite is capable of providing a reliable and accurate estimate of the intensity of the magnetic fields it experienced as it cooled. Hence, it has the potential to provide a relatively well-constrained estimate of the formation distance of its parent body. As such, this meteorite could provide relatively robust constraints on the distances of the migration of solids with a wide range of sizes during the early solar system.

## 2. Samples and Methods

### 2.1. WIS 91600 Magnetic Petrology

Petrographic and X-ray diffraction measurements demonstrate that WIS 91600 contains magnetite, pyrrhotite, and trace amounts of FeNi metal (Rubin et al. 2007; Choe et al. 2010; Tonui et al. 2014; Howard et al. 2015; Yamanobe et al. 2018). Magnetite is the most abundant magnetic phase present at 6.5 vol% of all of the material in the meteorite, making it significantly more abundant than magnetite in the CM chondrites (Howard et al. 2015). Sulfides make up 3.5 vol% of all of the material in WIS 91600; this includes pyrrhotite (which can be either magnetic or nonmagnetic depending on its composition), pentlandite (which is nonmagnetic), and troilite (which is also nonmagnetic; Rochette et al. 2008; Howard et al. 2015). FeNi metal is typically found as a limited number of small grains (typically  $\lesssim 1 \mu\text{m}$ , but can reach several micrometers in size) within some olivine and pyroxene crystals in a handful of chondrules (Rubin et al. 2007), and is very much a trace mineral ( $\sim 0\text{--}0.2$  vol% of the material in the meteorite inferred from X-ray diffraction and petrographic observations; Howard et al. 2015). Based on these observations, we expect that the predominant magnetic carrier in WIS 91600 is magnetite.

Magnetite is found in a variety of morphologies, including euhedral grains typically  $< 10 \mu\text{m}$ , stacked platelets each  $< 10 \mu\text{m}$  in diameter, and framboids composed of thousands of tessellated  $\lesssim 500$  nm sized grains (Tonui et al. 2014; Yamanobe et al. 2018). Pyrrhotite exists as isolated  $< 200$  nm grains, aggregates of  $\lesssim 1 \mu\text{m}$  grains, and a handful of  $\sim 50 \mu\text{m}$  grains containing blebs of pentlandite (Tonui et al. 2014). Magnetic particles smaller than a few micrometers typically make stable paleomagnetic recorders, with micromagnetic

calculations indicating that particles that contain magnetic vortices (those that are typically a few hundred nanometers; Kimura et al. 2013) can reliably record and preserve magnetic remanences for hundreds of billions of years (Nagy et al. 2017). Indeed, magnetite-bearing meteorites have previously been found to be high-fidelity paleomagnetic recorders (Cournede et al. 2015; Gattacceca et al. 2016), with some subsamples of such meteorites being able to record and preserve paleointensities as weak as  $0.15 \mu\text{T}$  (Bryson et al. 2020).

### 2.2. WIS 91600 Subsamples

We cut 13 interior and two fusion-crust mutually oriented subsamples of WIS 91600,79 (1.7 g), which was loaned to us from the Antarctic Search for Meteorites (ANSMET) collection. We cut all of our subsamples using a dry wire saw in the magnetically shielded room in the Massachusetts Institute of Technology (MIT) Paleomagnetism Laboratory. All interior subsamples were  $> 4.4$  mm from the fusion crust and were each 1–3 mm in size. Our fusion-crust subsamples carried fusion crust along one edge and extended  $< 1$  mm from this edge into the interior. We measured the remanence carried by all of our subsamples using a 2G Enterprises Superconducting Rock Magnetometer 755 in a class  $\sim 10,000$  magnetically shielded room in the MIT Paleomagnetism Laboratory.

### 2.3. AF Demagnetization

We AF-demagnetized five interior subsamples using an automated procedure that sequentially applied AFs with increasing peak intensity up to 145 mT in 150 steps (Kirschvink et al. 2008). For each intensity, we applied AFs along three orthogonal directions and measured the magnetization remaining after the application of each AF. We averaged the three magnetizations measured at each applied field intensity to mitigate the effects of gyroremanent magnetizations and spurious ARMs following the Dunlop–Zijderveld method (Stephenson 1993). We additionally demagnetized one subsample (WIS.1) up to 270 mT.

We estimated the paleointensity of the field experienced by WIS 91600 by applying and subsequently demagnetizing ARMs in the laboratory with a peak AF intensity of 260 mT and a bias field intensity of  $50 \mu\text{T}$  to all interior AF subsamples. We calculated the ARM paleointensity,  $B_{\text{ARM}}$ , using:

$$B_{\text{ARM}} = \frac{\Delta\text{NRM } B}{\Delta\text{ARM } f'} \quad (1)$$

where  $\Delta\text{NRM}$  is the change in NRM over a given coercivity range,  $\Delta\text{ARM}$  is the change in ARM over the same coercivity range,  $B$  is the intensity of the laboratory bias field, and  $f'$  is the value of TRM/ARM, which accounts for the different recording efficiencies of TRMs and ARMs. The average of this last value is 3.33 for magnetite and is unknown for pyrrhotite (Weiss & Tikoo 2014). We chose to adopt a value of 3.33 for pyrrhotite, which introduces an obvious uncertainty to our recovered  $B_{\text{ARM}}$  values. We also applied and demagnetized an IRM acquired in a 250 mT field to our interior AF subsamples and calculated the IRM paleointensity,  $B_{\text{IRM}}$ ,

using:

$$B_{\text{IRM}} = \frac{\Delta\text{NRM}}{\Delta\text{IRM}}a \quad (2)$$

where  $\Delta\text{IRM}$  is the change in IRM over a given coercivity range, and  $a$  is a calibration factor with units of field intensity (average of  $2500 \mu\text{T}$  for magnetite; Weiss & Tikoo 2014; and  $500\text{--}3000 \mu\text{T}$  for pyrrhotite depending on grain size; Gattacceca & Rochette 2004; Kletetschka & Wieczorek 2017). We calculated the ratios of the remanences by fitting a straight line to the two data sets across a given coercivity range. The 95% uncertainty values we quote are the formal errors in this fitting procedure. The values of  $f$  and  $a$  are likely uncertain to a factor of one to five (Gattacceca & Rochette 2004; Weiss & Tikoo 2014).

#### 2.4. Thermal Demagnetization

We performed double heating paleointensity measurements on seven interior subsamples. We adopted the alternating in-field, zero-field (IZZI) protocol (Tauxe & Staudigel 2004), performing pTRM checks between every zero-field and in-field step. We heated the subsamples from  $100^\circ\text{C}$  to  $200^\circ\text{C}$  in  $20^\circ\text{C}$  steps, then from  $200^\circ\text{C}$  to  $330^\circ\text{C}$  in  $10^\circ\text{C}$  steps and finally from  $330^\circ\text{C}$  to  $390^\circ\text{C}$  in  $20^\circ\text{C}$  steps (our subsamples all displayed significant thermal alteration at temperatures  $>390^\circ\text{C}$ ). We performed the in-field steps in a  $20 \mu\text{T}$  field. We performed all heating steps in air using an ASC Scientific TD48-SC oven in the magnetically shielded room in the MIT Paleomagnetism Laboratory. We calculated the double heating paleointensity,  $B_{\text{dh}}$ , using:

$$B_{\text{dh}} = \frac{\Delta\text{NRM}}{\Delta\text{pTRM}}B \quad (3)$$

where  $\Delta\text{pTRM}$  is the change in laboratory pTRM gained during the measurements. We calculated  $\Delta\text{NRM}$  in this case using vector subtraction to place the last point in the temperature range of interest on the origin. Due to the relatively friable nature of WIS 91600, we mounted our subsamples in 6 mm diameter nonmagnetic quartz tubes and packed them with nonmagnetic quartz wool so we did not have to handle the subsamples directly during our measurements. We AF-demagnetized the whole sample holding assemblage (quartz tube and wool) prior to adding the subsamples such that they had moments  $<1 \times 10^{-11} \text{ A m}^2$ . Due to having to detach and re-attach the quartz tubes to the quartz disks between each measurement to conduct the heating, this approach yielded larger mean angular deviation (MAD) values and larger scatter among the thermal paleodirections recovered from the different subsamples compared to our AF subsamples, which remained immobilized during their demagnetization. Additionally, we thermally demagnetized one subsample (WIS.6) in the absence of a field up to  $390^\circ\text{C}$ .

#### 2.5. Magnetic Characterization

We measured hysteresis loops of two of our AF subsamples (WIS.1 and WIS.2) as well as a first-order reversal curve (FORC) diagram of WIS.2 to characterize their remanence carriers. We performed these measurements after this subsample had its NRM and laboratory remanences removed. We

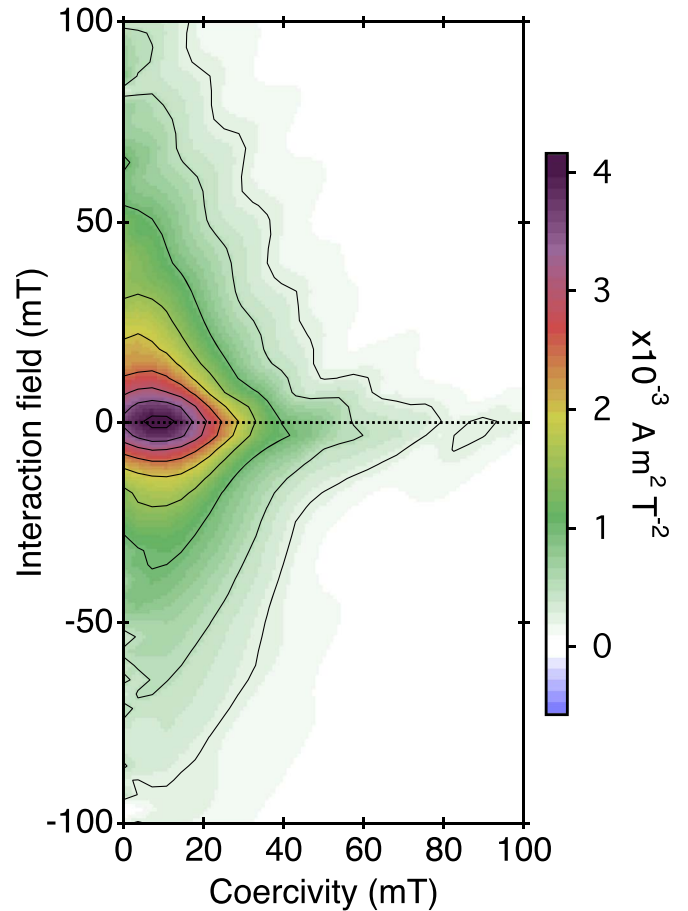


**Figure 1.** First-order reversal curve (FORC) diagram of WIS.2. The diagram shows a distinctive triangular shape. The FORC distribution extends vertically to interaction fields of  $\pm\sim 100$  mT at low coercivities and horizontally to a coercivity of  $\sim 100$  mT at near-zero interaction fields. The diagram contains a peak at  $H_c \approx 10$  mT and  $H_u \approx 0$  mT.

conducted these measurements using a Lake Shore Cryotronics PMC MicroMag 3900 series alternating gradient field magnetometer at the University of Cambridge. We measured 243 FORCs with a  $2.4$  mT step size,  $200$  ms averaging time, and a saturating field of  $0.7$  T. We processed the FORC diagrams using the VARIFORC approach (Egli 2013) built into the FORCinel software package (Harrison & Feinberg 2008). We used a vertical ridge smoothing factor ( $S_{c0}$ ) of seven, a horizontal smoothing factor ( $S_{c1}$ ) of ten, a central ridge smoothing factor ( $S_{b0}$ ) of seven, a vertical smoothing factor ( $S_{b1}$ ) of ten, and horizontal and vertical  $\lambda$  values of  $0.1$  during this processing.

### 3. Results

#### 3.1. Magnetic Characterization

The FORC diagram of WIS.2 (Figure 1) displays a triangular shape with a peak at coercivity  $H_c \approx 10$  mT and interaction field  $H_u \approx 0$  mT. It is very similar to that measured from a Tagish Lake subsample (Bryson et al. 2020).

The shape of the FORC distribution can be used to recover the mineralogy and predominant domain state of the magnetic carriers within a sample. Multi-domain grains typically display vertical FORC distributions that have high intensities at low coercivity values (typically  $<10$  mT) that spread up to high interaction field values ( $>100$  mT), display contours parallel to

the vertical axis, and can display a small peak on the origin (Roberts et al. 2017; Harrison et al. 2018). The contours in the FORC diagram of WIS 91600 are not parallel to the vertical axis and its peak is not on the origin, arguing that the predominant magnetic carriers in WIS 91600 are not multi-domain grains. Magnetic remanences carried by multi-domain grains can be relatively easily overwritten by prolonged exposure to the Earth’s magnetic field and/or lost during the  $\sim 4.5$  Gyr between a meteorite being magnetized and landing on Earth. Fortunately, these grains appear to be a minor component of the magnetic material in WIS 91600. Instead, the shape of the FORC diagram and the position of its peak match those measured from samples of tightly clustered, magnetically interacting single-domain and/or vortex-state particles of magnetite (Muxworthy & Dunlop 2002; Harrison & Lascu 2014). Specifically, the shape and peak position of this FORC diagram are intermediate between those of tightly clustered magnetite powders with grain sizes of 1.7 and 7  $\mu\text{m}$  (Muxworthy & Dunlop 2002). The close proximity of the magnetite particles in the framboids (Tonui et al. 2014; Yamanobe et al. 2018; and, to a slightly lesser extent, the stacked platelets) means that we expect that these particles are magnetically interacting (Evans et al. 2006), and so are likely the predominant magnetic phase in WIS 91600. This observation matches the high abundance of framboids observed in petrographic studies (Rubin et al. 2007; Choe et al. 2010; Tonui et al. 2014; Yamanobe et al. 2018). Electron holography imaging of particles in meteoritic magnetite framboids demonstrates that these particles adopt vortex domain states (Kimura et al. 2013), supporting the conclusion drawn from the FORC diagram. Vortex states have recently been demonstrated to be capable of preserving magnetic remanences for well over the age of the solar system (Nagy et al. 2017). As such, we believe that the remanence carried by WIS 91600 is a reliable record of the magnetic fields experienced by this meteorite after it was impact heated during the early solar system. FORC diagrams of separated vortex-state particles also show some vertical spreading (Roberts et al. 2014; Harrison et al. 2018), so it is likely that a portion of the vertical spreading observed in the FORC diagram of WIS.2 is due to the presence of vortex-state particles, as well as interactions between tightly packed grains.

The FORC signature of single-domain and pseudo-single-domain pyrrhotite particles tends to display an elliptical distribution with a peak at a coercivity value of 15–80 mT and at slightly negative interaction field values (Wehland et al. 2005; Roberts et al. 2006). This peak moves to lower coercivity values within this range as the pyrrhotite grain size increases (from  $< 5 \mu\text{m}$  to  $\sim 40 \mu\text{m}$ ) and likely transition from more single-domain-dominated behavior to more pseudo-single-domain-dominated behavior (Wehland et al. 2005). As there is no clear signal corresponding to the expected signature of pyrrhotite in the FORC diagram of WIS.2, we conclude that single-domain/vortex-state magnetic pyrrhotite is a minor component of the magnetic grains in WIS 91600. This observation explains why we do not see a pronounced change in magnetization on heating through the Curie temperature of pyrrhotite (290°C–320°C; see Section 3.4). However, our AF demagnetization measurements indicate that, although a minor component, pyrrhotite does appear to carry a remanence (see Section 3.2). FORC diagrams of pyrrhotite-bearing samples often also extend to higher coercivity values than those of

magnetite-bearing samples (Wehland et al. 2005; Roberts et al. 2006, 2014). The FORC distribution from WIS.2 extends to slightly higher coercivity values ( $> 100$  mT) than that observed in Tagish Lake, possibly reflecting a higher relative abundance of magnetic pyrrhotite compared to magnetite in WIS 91600 than in Tagish Lake.

The similarity of the magnetic carriers among a suite of samples can be assessed through their hysteresis properties. Figure 2(a) shows the AF demagnetization of the IRM applied to all five AF subsamples. These curves are proxies for the coercivities of the particles within a sample; the absolute value on the vertical axis depends on the amount of magnetic material present as well as its domain state, and the extent along the horizontal axis depends on the distribution of the coercivities of the particles within a sample. All five of these curves are very similar (significantly more similar than those measured from different CM chondrites; Cournede et al. 2015) demonstrating that the properties of the magnetic carriers in all of our subsamples are almost identical. Table 1 shows the mean destructive field (MDF; field intensity required to reduce the ARM or IRM by a factor of two) for all five subsamples. Again, the values are very similar among the five subsamples as well as between the ARM and IRM methods, further supporting very similar magnetic carriers among all of our subsamples. Figure 2(b) shows the ratio of the saturation remanence magnetization ( $M_{rs}$ ) to the saturation magnetization ( $M_s$ ) against the ratio of the coercivity of remanence ( $B_{cr}$ ) to the coercivity ( $B_c$ ; known as a Day plot) recovered from hysteresis loop measurements of two WIS 91600 subsamples. Again, these hysteresis properties are very similar for both subsamples, further supporting a high degree of similarity among the magnetic mineralogy in our WIS 91600 subsamples. Moreover, these points plot in the pseudo-single-domain region of the Day plot. Although the relevance of this has recently been questioned (Roberts et al. 2018), this observation suggests that the bulk magnetic properties of the subsample could be dominated by vortex-state particles, consistent with microscopy observations (Kimura et al. 2013) and our FORC diagram (Figure 1). This observation further supports a high stability for the magnetic recorders in WIS 91600.

### 3.2. AF Demagnetization

The interior subsamples of WIS 91600 all display a loss in their NRM up to AF intensities of 145 mT (Figures 3(a) and 4, Table 2), while WIS.1 (which we demagnetized to an AF intensity of 270 mT) displays minimal loss of its NRM at AF intensities  $> 145$  mT. These NRMs contain three components: one at low coercivity (LC; 0 to 3.0–8.5 mT); one at medium coercivity (MC; 3.0–8.5 to 8.5–35 mT); and one at high coercivity (HC; 8.5–35 to 145 mT). These components were identified by changes in the direction of the remanence in the individual orthogonal projection diagrams during AF demagnetization of the NRM carried by each subsample (Figure 4). The LC components are randomly oriented (length of the vector sum  $R = 2.8$  for  $N = 5$  samples) while the MC and HC components are each uniform ( $R = 4.8$  and  $R = 4.9$ , respectively,  $N = 5$ ) and are similarly oriented, overlapping within their  $\alpha_{95}$  confidence intervals (Figure 5). However, the orthogonal projection diagrams (Figure 4) demonstrate that a distinct change in the direction of the remanence during AF demagnetization exists at the MC–HC transition in each of the five AF subsamples, arguing that the MC and HC components

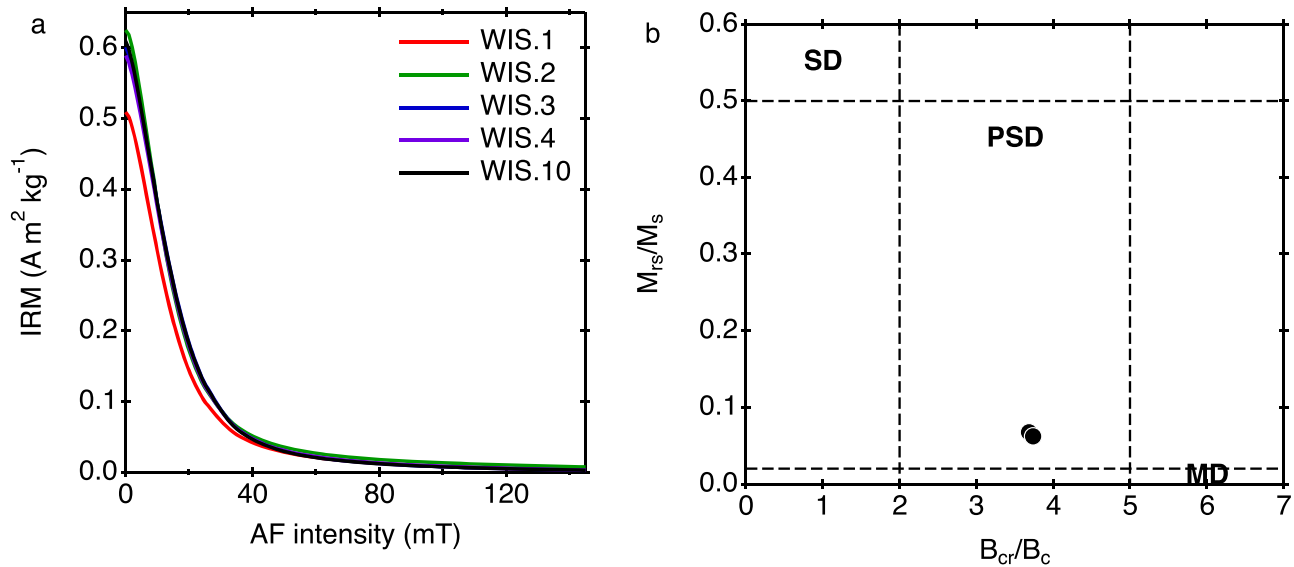


**Figure 2.** (a) Mass normalized isothermal remanent magnetization as a function of alternating field (AF) intensity for all five AF subsamples. (b) The ratio of the saturation remanence magnetization ( $M_{rs}$ ) to the saturation magnetization ( $M_s$ ) against the ratio of the coercivity of remanence ( $B_{cr}$ ) to the coercivity ( $B_c$ ) for WIS.1 and WIS.2. SD: single-domain; PSD: pseudo-single-domain; MD: multi-domain.

**Table 1**

Mean Destructive Field (MDF) for Our Five AF Subsamples Calculated from Their IRM and ARM AF Demagnetizations

Subsample	MDF of IRM (mT)	MDF of ARM (mT)
WIS.1	12.8	15.8
WIS.2	12.6	15.0
WIS.3	13.4	17.4
WIS.4	13.4	16.7
WIS.10	13.2	17.2

are in fact distinct (e.g., Figure 4). This observation is reinforced by the fact that none of the MC components are origin-trending while all of the HC components do trend toward the origin (arguing that the MC and HC components have different directions and, as such, are distinct components). Furthermore, the angle between the MC and HC components is larger than the MAD of the MC component in all of our AF subsamples (Table 2), demonstrating that the direction of each MC component is distinct from the direction of each HC component. The MAD values of the HC components are typically larger than those of the MC components due to the relatively weak paleointensity carried by the HC component (see Sections 3.3 and 3.5) and the AF demagnetization procedure, which randomized the domain configuration within the magnetic grains during the application of each applied field and added scatter to the data. However, two AF subsamples (WIS.1 and WIS.4) display noticeably smaller HC MAD values ( $\leq 7^\circ$ ). The directions of the MC and HC components for both of the subsamples do not overlap within the 95% confidence interval of both the MC and HC components, further arguing that the MC and HC directions carried by each subsample are distinct. Together, all of these observations argue that each subsample of WIS 91600 carries distinct MC and HC components that are similarly oriented but are resolvable in the AF demagnetization data. As such, the overlap in the average MC and HC directions is likely a result of the

comparatively large scatter in the individual directions of the MC components (which cause a relatively large  $\alpha_{95}$  value for the average MC component) combined with the similar orientations of the individual MC and HC components recovered from the demagnetizations of each subsample. Together, these properties make an overlap between the average directions of these two components likely, even when the individual demagnetizations support each subsample carrying multiple separate components with distinct directions.

The LC component is carried by grains with the lowest coercivities and shortest relaxation times and, as such, is almost certainly a viscous remanent magnetization (VRM) imparted at low temperature by Earth's field during recent sample handling (potentially imparted during the meteorite's residence at Johnson Space Center and/or shipping to MIT).

The remanences carried by our fusion-crust subsamples consist of a single component and are approximately an order of magnitude stronger than those carried by the interior subsamples (Table 2). This remanence is a record of the Earth's magnetic field experienced by WIS 91600 as its surface cooled following heating during atmospheric entry. The average direction of the component in the fusion-crust subsamples is broadly similar to the average MC and HC directions, but importantly does not overlap within 95% uncertainty with either of these directions, arguing that neither the MC nor HC components are pTRMs acquired following atmospheric entry (Figure 5(b)). This observation is reinforced by the large distance of some of our subsamples from the fusion crust (up to  $\sim 9$  mm; Table 2), which is much larger than the distance in the interior of a meteorite that is typically heated by atmospheric entry ( $\lesssim 2$  mm; Weiss et al. 2010). The MC and HC remanences are also very unlikely to have been imparted by a hand magnet because we would expect such remanences to be significantly (at least one to two orders of magnitude) stronger. Instead, because the MC component is carried by grains with intermediate coercivities and relaxation times, it is possible that this component could correspond to a VRM imparted at low temperature by the Earth's field during the meteorite's prolonged residence in Antarctica prior to collection. This

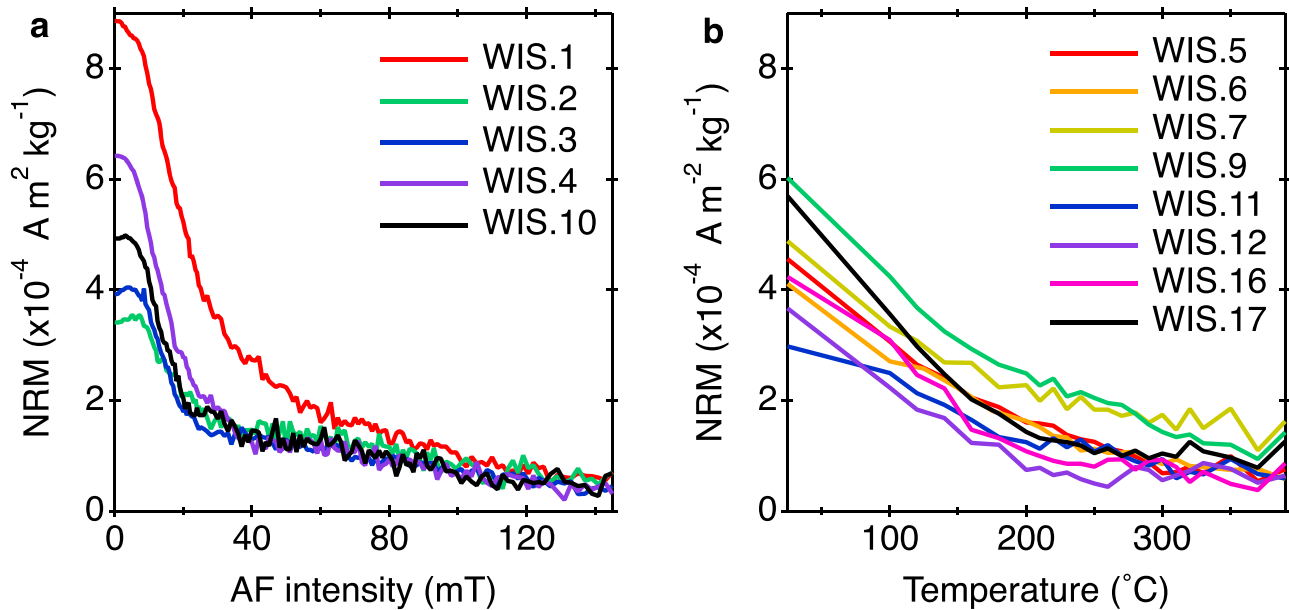


**Figure 3.** Demagnetization of the NRM carried by (a) AF subsamples and (b) thermal subsamples as a function of AF intensity and temperature, respectively.

observation is supported by the recovered low-temperature paleointensity, which is very similar to that of the geomagnetic field (see Section 3.5). In this scenario, the MC component could be a rounding of the HC component and the component carried by the fusion-crust subsamples. If this is the case, the origin of the MC component would differ from that of the HC component, further justifying our classification of these two components as distinct. Furthermore, the broadly similar directions of the fusion-crust component and the HC component would cause the average MC component to be very similarly oriented to HC component, explaining the overlap in the average recovered directions of these two components. Additionally, the MC component could also be a rounding of the HC and LC components resulting from the nature of AF demagnetization (which can effectively blur two components across their transition). Again, in this case, the MC component would be similarly oriented to the HC component and would contain a terrestrial contamination, arguing that it should be treated as distinct from the HC component.

The HC component is origin-trending in all of our subsamples (Figure 4, Table 2). These directions were not forced to the origin. This observation argues that this HC remanence could be primary (i.e., pre-terrestrial). The large value of the upper limit of our HC AF range (145 mT) demonstrates that the NRM in our subsamples is carried by very stable grains with relaxation times on the order of tens to hundreds of billions of years (Nagy et al. 2017). Given the likely residence time of WIS 91600 on Earth (the average residence time for Antarctic meteorites is  $\sim 100$  kyr; Bland et al. 2006), it is extremely unlikely that these grains could have been viscously magnetized by the Earth’s magnetic field. This result is supported by the weak recovered HC and high-temperature paleointensities that are approximately an order of magnitude weaker than Earth’s field (see Sections 3.3 and 3.5). As such the properties of the HC remanence carried by our interior subsamples are inconsistent with a terrestrial overprint and instead suggest that this remanence is pre-terrestrial and happens to be similarly oriented to that carried by the fusion crust.

### 3.3. ARM and IRM Paleointensities

Figure 6 shows the demagnetization of the NRM carried by WIS.3 as a function of the demagnetization of its ARM and IRM. These curves display a relatively steep slope between AF intensities of 0 and  $\sim 25$  mT, which then flattens between  $\sim 25$  and  $\sim 75$  mT, before increasing sharply between  $\sim 75$  and 145 mT. FORC diagrams of magnetite powders tend to display peaks at relatively low coercivities ( $< 50$  mT depending on grain size; Muxworthy & Dunlop 2002) and a weaker signal that can extend up to  $\sim 300$  mT. FORC diagrams of samples bearing single-domain pyrrhotite grains tend to display peaks at  $\sim 15$ – $80$  mT and a weaker signal that extends up to  $\sim 500$  mT (Dekkers 1988; Wehland et al. 2005; Roberts et al. 2006). As such, pyrrhotite tends to display higher coercivities than magnetite. Therefore, we expect that the remanence carried by grains with lower coercivity in a sample that contains magnetite and pyrrhotite to be dominated by magnetite, and the remanence carried by grains with higher coercivity in such a sample to be dominated by pyrrhotite. As such, we interpret the changes observed during our NRM demagnetizations at AF intensities  $> 25$  mT as the sequential unblocking of the HC component of the remanences carried by magnetite and pyrrhotite, respectively. WIS 91600 was heated to between  $400^\circ\text{C}$  and  $500^\circ\text{C}$  on its parent body (Yabuta et al. 2010; Cloutis et al. 2012; Tonui et al. 2014), which is below the Curie temperature of magnetite ( $580^\circ\text{C}$ ; Rochette et al. 2008). Hence, we expect that only  $\sim 12.5\%$ – $25\%$  of the magnetite grains (based on thermal demagnetization of TRMs applied to the magnetite-bearing CV chondrite Kaba; Gattacceca et al. 2016) were magnetized when WIS 91600 cooled following this heating. On the other hand, the Curie temperature of pyrrhotite is  $290^\circ\text{C}$ – $320^\circ\text{C}$  (Rochette et al. 2008), so we expect that all of the pyrrhotite grains were magnetized following this heating. The peak AF intensity used to impart our ARMs and the magnitude of our IRMs are greater than the highest coercivity observed in the FORC diagram of WIS.2 (Figure 1), indicating that these laboratory remanences were imparted to all of the grains in our subsamples. Hence, we expect the change in the pTRM carried by magnetite to be relatively small compared to



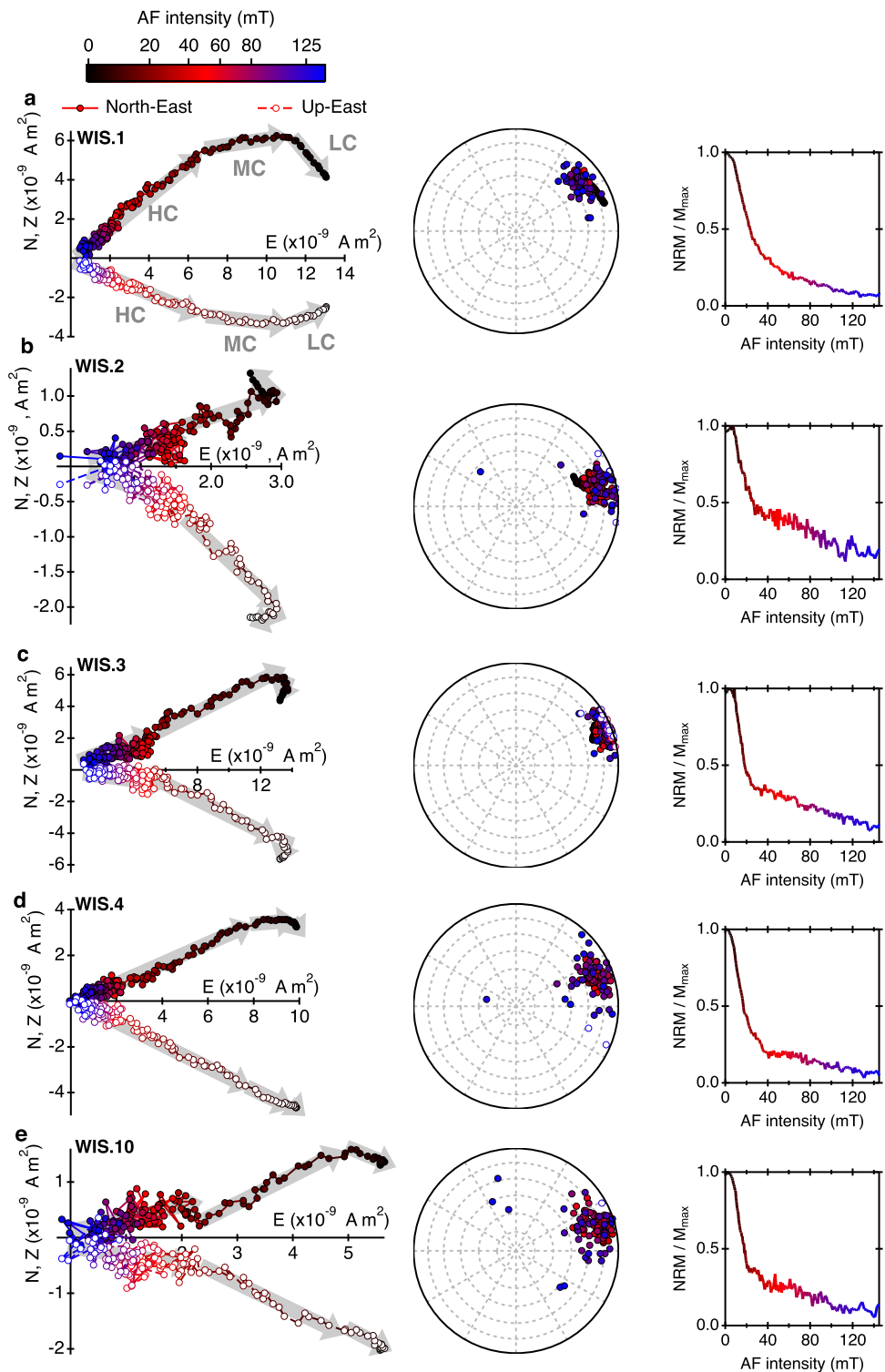


**Figure 4.** Alternating field (AF) demagnetization of the NRM carried by our AF subsamples. Shown on the left are orthogonal projections of the end points of the NRM vectors onto the North-East (filled points) and Up-East (open points) planes during AF demagnetization. The gray arrows depict the directions of the LC, MC, and HC components. Shown in the center is the direction of the NRM vector that remains after the application of increasingly intense alternating fields in an equal area stereographic projection. The intensity of the alternating field is depicted by the color scale. Shown on the right is the variation of the NRM normalized to the maximum magnetization value ( $M_{max}$ ) as a function of applied AF intensity.

the changes in the ARM and IRM imparted to this mineral (because only a fraction of the magnetite grains carry the pTRM while all of the grains carry the ARM and IRM). On the other hand, we expect the change in the pTRM carried by pyrrhotite to be relatively large compared to the changes in the

ARM and IRM imparted to this mineral (because all of the pyrrhotite grains carry the pTRM and the ARM and IRM). These effects are expected to manifest themselves as shallower slopes in Figure 6 for magnetite-dominated remanences compared to pyrrhotite-dominated remanences. The change in

**Table 2**  
Properties of the AF Demagnetization of WIS 91600

Subsample		Mass (mg)	Distance from Fusion Crust (mm)	NRM ( $\times 10^{-3}$ A m <sup>2</sup> kg <sup>-1</sup> )	ARM ( $\times 10^{-3}$ A m <sup>2</sup> kg <sup>-1</sup> )	IRM (A m <sup>2</sup> kg <sup>-1</sup> )	Last AF Step/NRM	AF Range (mT)	$N^a$	MAD (°) <sup>b</sup>	dANG (°) <sup>c</sup>	MAD > dANG?	Decl. (°) <sup>d</sup>	Inc (°) <sup>e</sup>	Angle between MC and HC Components (°)
WIS.1	LC	15.7	8.3	0.89	2.86	0.51	0.080	NRM–7.5	15	4.0	75.4	N	138.6	14.1	31.4
	MC							7.5–17	20	6.6	25.3	N	79.8	–5.2	
	HC							17–145	117	6.2	3.4	Y	51.4	–20.4	
WIS.2	LC	10.5	8.3	0.34	3.24	0.62	0.204	NRM–8	16	22.0	76.4	N	307.4	–17.0	21.1
	MC							8–27	37	14.9	18.6	N	75.6	–45.7	
	HC							27–145	99	25.3	8.3	Y	75.0	–24.6	
WIS.3	LC	38.3	9.3	0.39	3.42	0.60	0.117	NRM–6.5	13	15.5	84.9	N	186.1	–42.6	19.5
	MC							6.5–24.5	37	8.9	16.1	N	67.4	–28.2	
	HC							24.5–145	102	21.1	3.8	Y	72.5	–9.3	
WIS.4	LC	17.7	6.8	0.64	3.25	0.59	0.049	NRM–3	6	13.3	72.6	N	152.2	–24.8	23.3
	MC							3–8.5	12	6.3	21.7	N	90.8	–17.3	
	HC							8.5–145	134	7.0	4.0	Y	67.0	–24.6	
WIS.10	LC	12.3	5.5	0.47	3.38	0.61	0.139	NRM–8.5	17	12.8	36.5	N	113.6	–30.2	19.6
	MC							8.5–20	24	6.7	12.8	N	63.7	–23.3	
	HC							20–145	111	22.9	9.7	Y	77.0	–8.4	
WIS.14 <sup>f</sup>		10.0	0	6.28	...	...	0.079	NRM–145	150	0.8	0.7	Y	40.9	–20.3	...
WIS.15 <sup>f</sup>		4.3	0	8.28	...	...	0.064	NRM–145	150	1.6	1.0	Y	44.1	–15.5	...
WIS.8 <sup>g</sup>		12.3	4.4	0.11	...	...	0.382	390°C–60	85	30.9	41.7	N	17.0	–37.4	...
WIS.11 <sup>g</sup>		12.2	8.7	0.06	...	...	0.446	390°C–45	70	31.7	64.01	N	21.8	–36.4	...

**Notes.**<sup>a</sup>  $N$ : number of points.<sup>b</sup> MAD: mean angular deviation.<sup>c</sup> dANG: deviation angle.<sup>d</sup> Decl.: declination.<sup>e</sup> Inc: inclination.<sup>f</sup> Fusion-crust subsamples.<sup>g</sup> AF demagnetization after heating to 390°C in zero field.

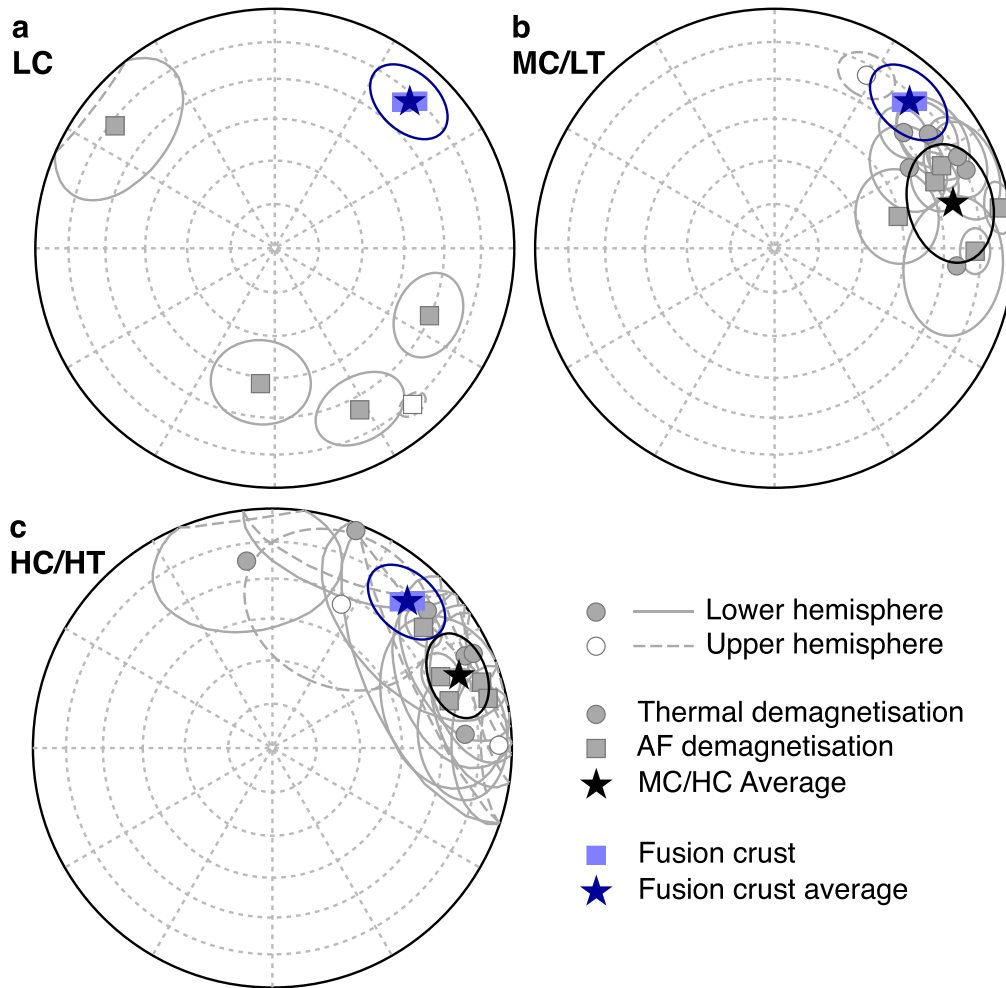


**Figure 5.** Equal area stereographic projections of the directions of (a) the LC component, (b) the MC and LT components, and (c) the HC and HT components of our subsamples. The components recovered from individual interior subsamples are shown by the gray points. The single components recovered from the fusion-crust subsamples are shown by the light blue points. The average MC and HC directions are depicted by the black stars in (b) and (c), respectively, and the average fusion crust direction is depicted by the dark blue star in (a)–(c). The ellipses around the directions recovered from the individual subsamples are MAD values of each subsample, and the ellipses around the average values are  $\alpha_{95}$  values.

slope in Figure 6 between  $\sim 25$  and  $75$  mT and at  $\gtrsim 75$  mT can, therefore, be explained by the thermal history of WIS 91600, and provides an independent constraint on the peak metamorphic temperature experienced by this meteorite (between the pyrrhotite and magnetite Curie temperatures).

Calibration factors are required to recover thermal-equivalent paleointensity values from ARM and IRM paleointensity methods ( $f'$  and  $a$  in Equations (1) and (2), respectively). These factors are calculated from total TRM measurements (i.e., when all of the grains are magnetized). As such, the documented values of these factors can only be used to estimate the paleointensity carried by total TRMs and will produce incorrect values for pTRMs. As such, we are only able to recover paleointensity estimates from the pyrrhotite in our subsamples. Any paleointensity calculated from the magnetite-dominated remanence would be an underestimate, as a much higher proportion of the magnetite grains in WIS 91600 will have been magnetized by our laboratory fields compared to the natural field, and the documented  $f'$  and  $a$  do not take this effect in account. We estimated the paleointensity carried by pyrrhotite in WIS 91600 by calculating paleointensities at AF intensities  $>75$  mT in an attempt to isolate the remanence carried just by this mineral. While pyrrhotite generally displays

higher coercivities than magnetite, it is possible for magnetite grains to display coercivities  $>75$  mT. This effect introduces another uncertainty to our recovered ARM and IRM paleointensities. Pyrrhotite grains with coercivities  $>75$  mT typically have sizes of  $<5 \mu\text{m}$  (Dekkers 1988), which correspond to  $a < 1500 \mu\text{T}$  in Equation (2) (Gattacceca & Rochette 2004). We, therefore, chose to calculate an upper limit on  $B_{\text{IRM}}$  using a value of  $a = 1500 \mu\text{T}$ . The paleointensity range recovered using this value of  $a$  includes the values that would be calculated using a value of  $a = 500 \mu\text{T}$ , which is the calibration factor suggested by a recent study (Kletetschka & Wieczorek 2017). Adopting  $a = 1500 \mu\text{T}$  produces an average upper limit of  $B_{\text{IRM}}$  of  $7.7 \pm 2.8 \mu\text{T}$  ( $1\sigma$ ). This value is within the error of the average  $B_{\text{ARM}}$  value of  $8.3 \pm 2.3 \mu\text{T}$  ( $1\sigma$ ) calculated using Equation (1) (Table 3). Given the number of considerable uncertainties associated with the calculation of these values (see Section 2.3), we believe they are likely within a factor of 10 of the actual thermal-equivalent paleointensity.

### 3.4. Thermal Demagnetization

Our thermal demagnetizations contain two resolvable components (Figures 3(b), 5, and 7): one at low temperature

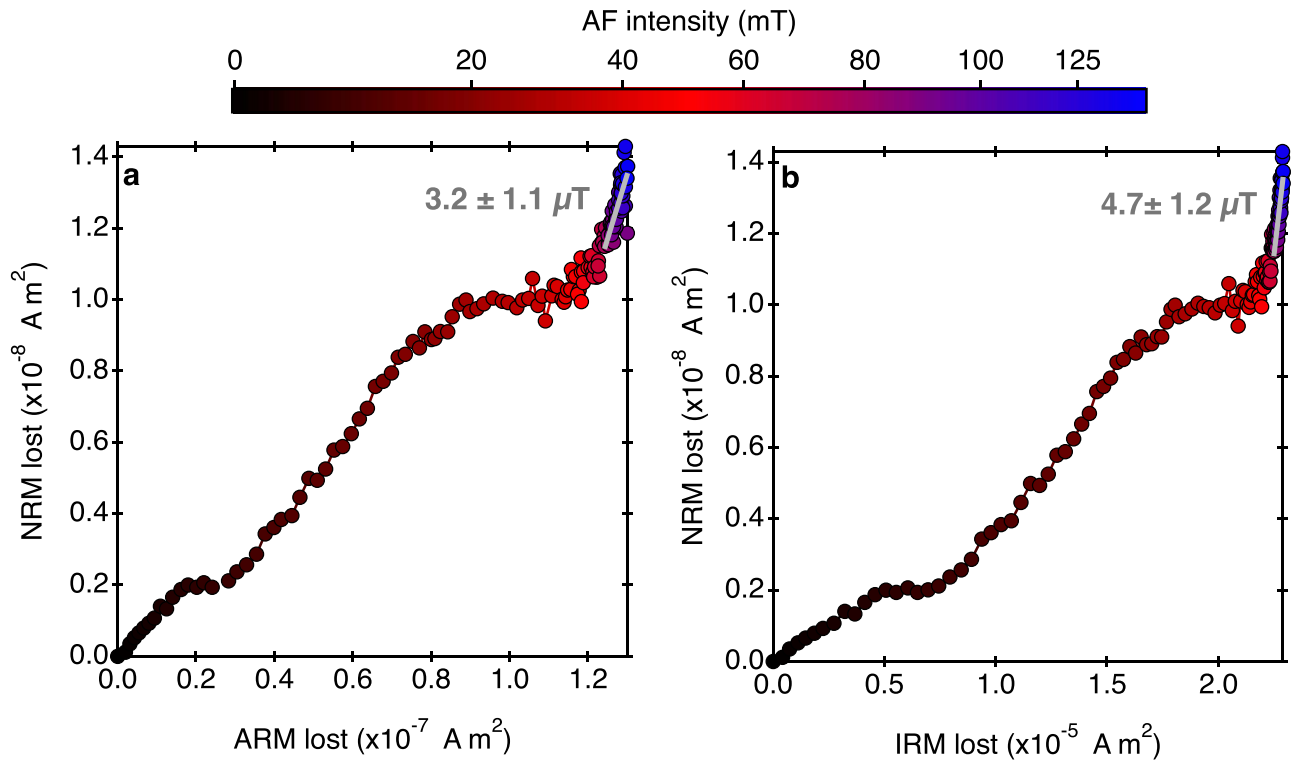


**Figure 6.** (a) ARM and (b) IRM paleointensity determination from WIS.3. The AF intensity is depicted by the color of the points according to the color bar. We recovered the HC paleointensity by fitting to the data at coercivities  $>75$  mT (gray line), which likely corresponds to the TRM carried predominantly by pyrrhotite. The shallower slope at coercivities between  $\sim 25$  mT and  $\sim 75$  mT likely corresponds to a pTRM carried predominantly by magnetite from which ARM and IRM paleointensities could not be reliably recovered.

**Table 3**

Recovered ARM Paleointensities and Upper List on IRM Paleointensities Recovered from Our AF Subsamples Using Equations (1) and (2), Respectively

Subsample	$B_{\text{ARM}}$ ( $\mu\text{T}$ )	$B_{\text{ARM}}$ 95% Uncertainty ( $\mu\text{T}$ )	$B_{\text{IRM}}$ ( $\mu\text{T}$ )	$B_{\text{IRM}}$ 95% Uncer- tainty ( $\mu\text{T}$ )
WIS.1	10.5	1.7	11.0	1.4
WIS.2	9.4	2.4	8.7	1.8
WIS.3	3.2	1.1	4.7	1.2
WIS.4	7.3	1.5	7.8	1.5
WIS.10	7.9	1.8	9.3	1.7

(LT; room temperature to  $200^{\circ}\text{C}$ – $220^{\circ}\text{C}$ ); and one at high temperature (HT;  $200^{\circ}\text{C}$ – $220^{\circ}\text{C}$  to at least  $320^{\circ}\text{C}$ – $370^{\circ}\text{C}$ ; Table 4). It is possible that a very low-temperature component (at  $\lesssim 100^{\circ}\text{C}$ ) could have been removed during the first one or two heating steps that could have been non-unidirectional and analogous to the LC component, but could not be resolved from the number of heating steps we conducted at these temperatures. The temperature defining the LT–HT transition corresponds to the change in direction of the NRM during thermal demagnetization identified in the orthogonal projection diagrams (Figure 7). The end of the HT range is defined by the last temperature step with minimal alteration (either in the form of small pTRM check values,  $\lesssim 10\%$ , or a coherent remanence direction). The LT and HT components are similarly oriented to each other and are both similarly oriented to the average MC and HC directions (Figure 5), suggesting a possible shared origin for the LT and MC components, and the HT and HC

components. Due to the scatter in the data, the limited number of steps, the relatively weak field intensity (see Section 3.5), and the similarity in direction between the LT and HT directions, the distinction between the LT and HT components is not as clear in some of our thermal subsamples as that between the MC and HC components in our AF subsamples (Figure 7). However, there is a distinct change in direction in many of our thermal subsamples at  $\sim 200^{\circ}\text{C}$ – $220^{\circ}\text{C}$  (e.g., WIS.16 and WIS.17), and we used the clear change in direction observed in all of the AF demagnetization measurements (which involved a far higher number of steps, immobilized samples, and no risk of alteration) as justification for identifying two components in the thermal demagnetization measurements where a change in direction is potentially more ambiguous (e.g., WIS.9, Figure 7(a)). The HT component is either origin-trending or close to being origin-trending (MAD and deviation angle [dANG] within  $2.5^{\circ}$  of each other) for five of the eight subsamples that were thermally demagnetized (Table 4). Again, these directions were not forced to the origin. We believe that the non-origin-trending nature of the HT component of some of our subsamples could be due to residual remanence from previous in-field paleointensity steps as a result of mild alteration during heating, pTRM tails, and the relatively large scatter introduced by our measurement procedure where we mounted the samples within quartz tubes (see Section 2.4). These effects also introduced relatively large scatter to the HT directions compared to the HC paleodirections (Figure 5(c)). As such, we chose not to include the LT or HT directions when calculating the average remanence directions, and we believe that the AF demagnetization data provide a much more reliable measure of the direction of the remanences carried by WIS 91600. Due to similar directions and remanence

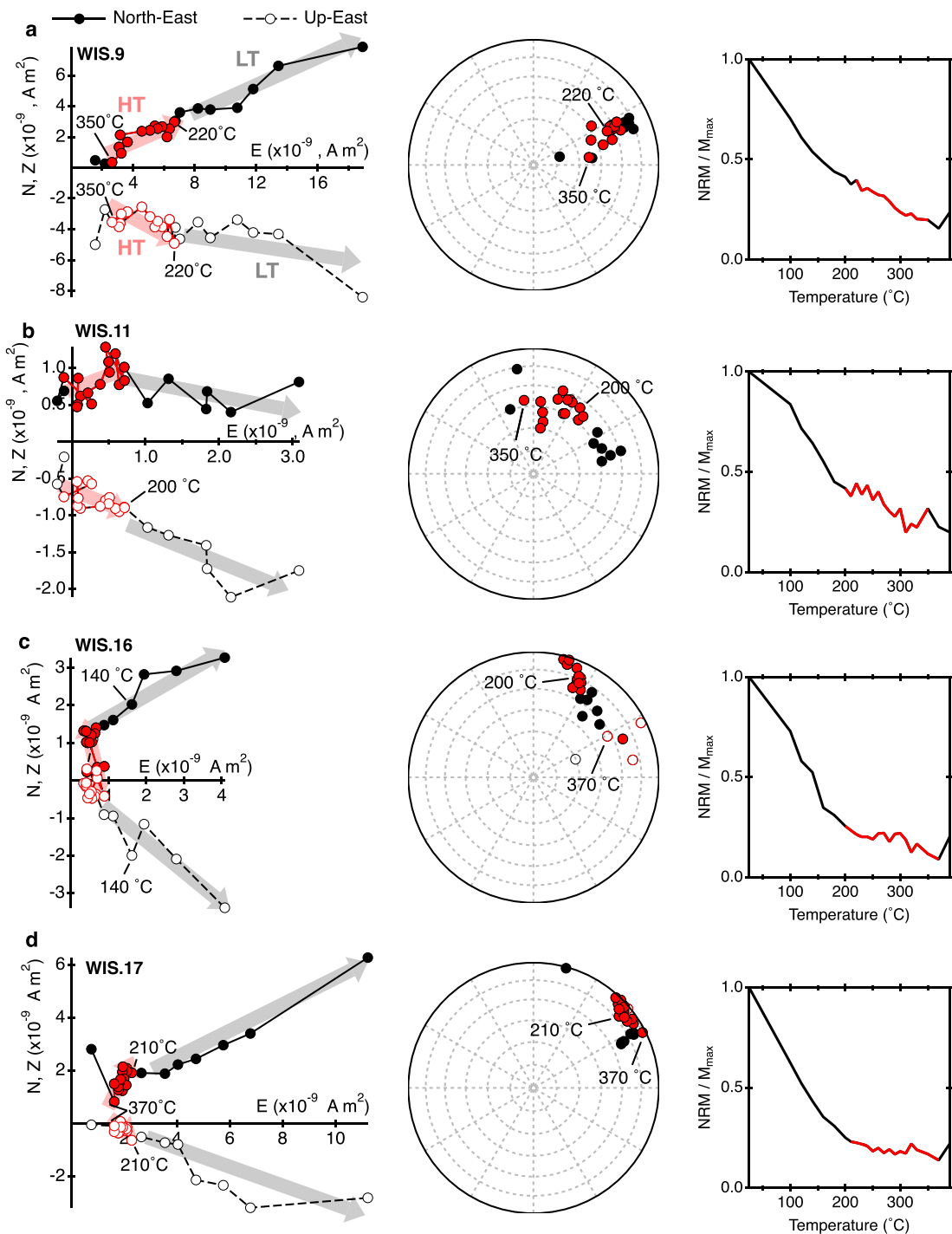


**Figure 7.** Demagnetization of the NRM carried by our thermal subsamples with low difference ratio sum (DRATS) values that did not display visibly low-quality demagnetizations. Shown on the left are orthogonal projections of the end points of the NRM vectors onto the North–East (filled points) and Up–East (open points) planes during thermal demagnetization. The LT components are shown by black points and gray arrows, and the HT components are shown by the red points and pink arrows. Shown in the center are stereographic projections of the direction of the NRM vector that remains after heating to increasingly higher temperatures. Shown on the right is the variation of the NRM normalized to the maximum magnetization value ( $M_{max}$ ) as a function of temperature.

magnitudes (Figure 3), we believe the LT remanence likely shares the same origin as the MC remanence (terrestrial overprint in the form of a VRM from prolonged exposure to Earth’s field that happens to be in a similar direction to the HT and HC remanence). Through the same arguments as the HC remanence (carried by very stable grains with very long relaxation times, weak paleointensity), we do not believe the

HT component is a terrestrial overprint, and is instead a pristine pre-terrestrial remanence.

We were able to constrain the peak temperature reached by WIS 91600 by comparing the magnitude of the thermal and AF demagnetizations (Figure 3, Tables 2 and 4). The ratio of the remanence remaining at the end of the HT range to the NRM falls between 0.09 and 0.38 among our different subsamples,

**Table 4**  
Properties of the Thermal Demagnetization of WIS 91600 Constructed from the Zero-field Steps in Our Double Heating Measurements (Paterson et al. 2014)

Subsample		Mass (mg)	Distance from Fusion Crust (mm)	NRM ( $\times 10^{-4}$ A m <sup>2</sup> kg <sup>-1</sup> )	Last Heating Step/ NRM	Temperature Range (°C)	$N^a$	MAD (°) <sup>b</sup>	dANG (°) <sup>c</sup>	MAD > dANG?	Decl. (°) <sup>d</sup>	Inc (°) <sup>e</sup>	Angle between LT and HT Components (°)	FRAC <sup>f</sup>	GAP-MAX <sup>g</sup>
WIS.5 <sup>h</sup>	LT	31.3	6.8	5.35	0.151	25–200	7	12.8	21.9	N	55.3	−20.1	28.7	0.56	0.36
	HT					200–330	14	18.5	17.9	Y	85.9	−20.4			
WIS.6 <sup>i</sup>	LT	18.0	6.8	4.12	0.141	25–200	7	10.5	14.0	N	53.4	−21.2	44.6	0.45	0.51
	HT					200–390	17	20.0	38.9	N	89.3	6.1			
WIS.7 <sup>h</sup>	LT	35.8	6.8	4.82	0.380	25–200	7	8.5	8.0	Y	27.9	19.3	14.7	0.37	0.48
	HT					200–350	15	29.6	25.0	Y	25.7	33.8			
WIS.9	LT	36.7	4.6	5.8	0.200	25–220	9	13.8	7.9	Y	67.8	−14.7	4.4	0.52	0.39
	HT					220–350	13	23.2	23.0	Y	64.4	−11.8			
WIS.11	LT	12.2	8.7	2.97	0.317	25–200	7	20.0	26.9	N	95.6	−24.6	45.2	0.40	0.28
	HT					200–350	15	32.3	34.8	N	48.5	−14.7			
WIS.12 <sup>j</sup>	LT	17.7	8.7	3.66	0.237	25–200	7	8.3	19.9	N	48.1	−28.4	39.9	0.45	0.40
	HT					200–330	14	43.9	77.3	N	64.8	−8.1			
WIS.16	LT	14.7	7.0	4.22	0.091	25–200	7	13.7	17.6	N	59.2	−34.8	59.2	0.54	0.29
	HT					200–370	16	26.9	37.2	N	352.2	−22.2			
WIS.17	LT	23.1	7.0	5.69	0.139	25–210	8	11.6	2.6	Y	63.4	−15.7	43.5	0.60	0.47
	HT					210–370	15	28.2	28.8	N	21.0	−3.1			

**Notes.**<sup>a</sup>  $N$ : number of points.<sup>b</sup> MAD: mean angular deviation.<sup>c</sup> dANG: deviation angle.<sup>d</sup> Decl.: declination.<sup>e</sup> Inc: inclination.<sup>f</sup> FRAC: relative fraction of the NRM demagnetized over the specified temperature range relative to the total NRM demagnetizes over the whole temperature range.<sup>g</sup> GAP-MAX: the largest fraction of the NRM lost between two adjacent temperature steps.<sup>h</sup> Subsamples with high difference ratio sum (DRATS) values.<sup>i</sup> Subsample heated to 390°C in the absence of a field.<sup>j</sup> Subsample with notably poorer quality thermal demagnetization.

**Table 5**  
pTRM Check Percent Values Measured during Double Heating Measurements

Preceding pTRM (°C)	pTRM Check (°C)	% between pTRM and pTRM check						
		WIS.5 <sup>a</sup>	WIS.7 <sup>a</sup>	WIS.9	WIS.11	WIS.12	WIS.16	WIS.17
140	100	-49.4	-28.5	-40.3	-26.9	-36.6	-25.5	-14.1
180	140	-29.9	-25.6	-27.4	-24.4	-29.8	-44.5	-25.0
210	180	-35.5	-30.1	-3.9	-17.3	-4.0	-20.3	-10.7
230	210	-9.5	-7.4	-8.1	-7.2	-10.5	-10.2	-12.9
250	230	-5.7	-12.4	-5.9	-8.1	-11.5	0.5	-2.4
270	250	-8.2	-4.7	-5.1	-5.2	-4.0	-5.4	-0.6
290	270	-5.5	-4.3	-0.9	-1.8	-0.7	1.0	4.0
310	290	1.6	-3.8	-2.1	-1.8	2.1	-2.3	-3.8
330	310	-3.9	-5.2	-2.5	-5.3	-5.6	-5.5	-7.2
370	330	-4.1	-8.2	-9.6	-13.0	-19.4	-4.8	-3.0

**Note.**

<sup>a</sup> Subsamples with high DRATS values.

while the ratio of the remanence remaining at the end of the HC range to the NRM values falls between 0.05 and 0.20. As our AF subsamples display minimal demagnetization above 145 mT (see Section 3.2), these ratios imply that heating to 330°C–370°C removed most of the pTRM carried by these subsamples. However, a small fraction of this pTRM likely still remained on heating to 330°C–390°C. We further explored this remanence by AF demagnetizing two subsamples (WIS.8 and WIS.11) after heating them in zero field to 390°C. This procedure allowed the remanence carried just by grains with blocking temperatures >390°C to be analyzed without risk of considerable alteration induced by heating to high temperatures. These subsamples both display weak losses in remanence that are broadly similarly oriented to the HC and HT components (Table 2). It is possible that the alteration induced in these samples by heating to 390°C caused a change in the direction and intensity of the remanence that remains at temperatures >390°C; however, we do not believe that this heating could have resulted in the measured moment being imparted to these subsamples. This observation indicates that WIS 91600 does carry a pTRM at blocking temperatures slightly greater than 390°C, in agreement with estimates of a peak metamorphic temperature somewhere between 400°C and 500°C. Importantly, the observation of a very weak remanence being carried at temperatures >390°C indicates that the subsamples that we thermally demagnetized were heated on their parent body to a similar temperature as that inferred from previous independent studies of WIS 91600.

### 3.5. Double Heating Paleointensities

To quantify the extent of chemical alteration induced in our subsamples during our double heating paleointensity experiments, we calculated the difference ratio sum (DRATS) parameter from our measured pTRM checks (Table 5). We calculated this parameter across the whole heating range from room temperature to the last temperature in the HT range (9–10 pTRM checks depending on the subsample). Although this is a relatively large number of pTRM checks and the DRATS value increases with this number, the values of this parameter are

similar to or less than the 25%–30% value that is typically acceptable for terrestrial samples (Tauxe et al. 2004; Tauxe & Staudigel 2004, Table 6) for five of the seven subsamples (average DRATS value <3.6% for these five subsamples). These values indicate that these five subsamples experienced minimal chemical alteration during heating. As such, we chose not to include the HT paleointensity of the two subsamples with high DRATS values when calculating the average HT paleointensity carried by WIS 91600. The HT quality factors ( $q$ ) calculated from our double heating experiments are >1 for all of our subsamples (Table 6), supporting our claim that they all carry HT remanences and that our recovered paleointensities are of relatively high quality (Paterson et al. 2014). However, the thermal demagnetization of one subsample (WIS.12) is of observably poorer quality than the others; once the LT component had been removed, the thermal demagnetization formed a scattered cluster very close to the origin, before jumping suddenly during one heating step (280°C) to form a new cluster of points slightly further from the origin over the remainder of the HT component. Consequently the MAD recovered from this subsample is particularly large (>40°), and the dANG value for this remanence is very large (77°3), indicating that it is far from being origin-trending (Table 4). As such, it is unclear that this subsample carries a resolvable HT component, probably because this particular subsample has a lower paleomagnetic fidelity than the others due to its specific mineralogy (Bryson et al. 2017). As such, we chose not to include the HT paleointensity of this subsample when calculating the average HT paleointensity carried by WIS 91600.

We recovered the paleointensities experienced by our double-heating subsamples of WIS 91600 by plotting their NRM remaining as a function of their pTRM gained during our heating measurements (known as an Arai plot) and calculating the slope of this curve across different temperature intervals (Figure 8). These plots show a change in gradient at the LT–HT transition. It is possible that a sample that carries a single NRM component can display two gradients in its Arai plot if the remanence is carried predominately by multi-domain grains;

**Table 6**  
Paleointensities and Quality Statistics Recovered from Our Double Heating Measurements of WIS 91600 (Paterson et al. 2014)

Subsample	DRATS (%)	LT Paleointensity ( $\mu\text{T}$ )	LT Paleointensity 95% Uncertainty ( $\mu\text{T}$ )	LT $\beta^a$	LT $q^b$	HT Paleointensity ( $\mu\text{T}$ )	HT Paleointensity 95% Uncertainty ( $\mu\text{T}$ )	HT $\beta^a$	HT $q^b$
WIS.5 <sup>c</sup>	66.8	38.6	16.0	0.21	2.44	11.7	2.3	0.098	5.18
WIS.7 <sup>c</sup>	43.9	25.8	3.5	0.068	9.92	3.2	1.1	0.17	2.20
WIS.9	28.2	37.9	6.9	0.091	7.90	8.5	0.9	0.053	10.61
WIS.11	32.3	19.2	6.6	0.17	4.10	3.2	1.1	0.17	2.79
WIS.12 <sup>d</sup>	30.6	26.0	10.4	0.20	3.60	3.4	1.4	0.21	1.92
WIS.16	35.1	36.6	18.0	0.25	2.28	3.7	1.0	0.14	4.17
WIS.17	21.6	44.7	4.7	0.053	14.97	2.3	1.1	0.24	1.95

**Notes.**

<sup>a</sup>  $\beta$  is the fraction of the standard error in the slope in the Arai diagrams relative to the absolute value of the slope.

<sup>b</sup>  $q = fg/\beta$  is a quality factor (measure of the quality of a paleointensity determination), where  $f$  is fraction of the NRM used to recover the paleointensity in a given temperature range and  $g$  is the gap factor.

<sup>c</sup> Subsamples with high DRATS values.

<sup>d</sup> Subsample with a notably low-quality thermal demagnetization.

the remanence carried by such grains can change over time due to their relatively low stability, which results in a curve in these plots (Paterson 2011). We do not believe this is the case in WIS 91600 for three reasons. First, there is a noticeable change in direction in Figure 4 at the point where the gradient changes in Figure 8, arguing that the remanence consists of two components that correspond to different paleointensities rather than one modified component. Second, our AF demagnetization measurements demonstrate that our subsamples carry multiple components, further indicating that the slope of the Arai plot can be explained by the sample having recorded multiple fields rather than carrying a single modified remanence. Third, our FORC and hysteresis measurements (Figures 1 and 2) argue that the predominant remanence carriers in these subsamples are interacting single-domain/vortex-states particles, which are thought not to show a pronounced change in gradient in their Arai plots over time. As such, our subsamples appear to have experienced different field intensities when they recorded their LT and HT remanences, rather than one component that changed over time.

The LT components from our subsamples with low DRATS values produce an average paleointensity of  $32.9 \pm 10.2 \mu\text{T}$  ( $1\sigma$ ; Table 6). The similarity of this value and the present-day geomagnetic field further argues that WIS 91600 carries a terrestrial overprint at low temperatures and low/medium coercivities. The average HT paleointensity from the four subsamples that produced low DRATS values and did not display notably low-quality thermal demagnetizations is  $4.4 \pm 2.8 \mu\text{T}$  ( $1\sigma$ ; Table 6). This value lies within the range recovered from the ARM and IRM paleointensity methods (Table 3). However, the HT paleointensity value is a significantly more reliable estimate of the field experienced by WIS 91600 due to the uncertainties associated with the ARM and IRM paleointensity recovery methods. One of our subsamples with a low DRATS value and high  $q$  value (WIS.9) produced a notably larger HT paleointensity than the other subsamples (Figure 8(b)).

## 4. Discussion

### 4.1. Origin of the Field That Magnetized WIS 91600

A number of field sources existed during the early solar system that could have imparted magnetic remanences to chondrites. These include the solar wind (Oran et al. 2018), impacts (Muxworthy et al. 2017), core dynamo activity (Bryson et al. 2019a), and the solar nebula (Fu et al. 2014, 2020; Cournede et al. 2015). The key parameters controlling which field was recorded by a specific chondrite are its peak temperature, cooling timescale, mechanism of heating, age of remanence acquisition, and aqueous alteration history.

There are a number of lines of evidence that WIS 91600 was heated to a peak temperature somewhere between  $400^\circ\text{C}$  and  $500^\circ\text{C}$  on its parent body (Nakamura 2005; Cloutis et al. 2012). These include X-ray absorption spectroscopy of IOM extracted from WIS 91600, which displays a poorly resolved  $1s-\sigma^*$  signal, indicating that this meteorite experienced short-lived heating (certainly shorter lived than that caused by radiogenic heating) to  $<500^\circ\text{C}$  (Yabuta et al. 2010). Moreover, the reflectance spectrum of WIS 91600 at wavelengths between  $0.3$  and  $3.6 \mu\text{m}$  matches that of Murchison (an aqueously altered CM2 chondrite that shares compositional and mineralogical similarities with WIS 91600) heated in the laboratory to between  $400^\circ\text{C}$  and  $500^\circ\text{C}$  (Tonui et al. 2014). Additionally, the concentrations of thermally labile elements (e.g., Cd) in WIS 91600 match those of Murchison heated to between  $400^\circ\text{C}$  and  $500^\circ\text{C}$  (Moriarty et al. 2009; Tonui et al. 2014). Moreover, transmission electron microscopy measurements of WIS 91600 demonstrate that it contains partially dehydrated phyllosilicates, which are thought to have lost their water on heating to  $400^\circ\text{C}$ – $500^\circ\text{C}$  (Tonui et al. 2014). Thermogravimetric analysis of WIS 91600 also demonstrates that it contains a relatively low amount of water in its hydroxides (carried at temperatures  $<400^\circ\text{C}$ ) compared to the CM chondrites, but a comparable amount of water carried by some phyllosilicates (carried at temperatures of  $400^\circ\text{C}$ – $600^\circ\text{C}$ ) as the CM chondrites, suggesting it was heated to slightly  $>400^\circ\text{C}$  on its parent body (Garenne et al. 2014). Raman spectroscopy also demonstrates that



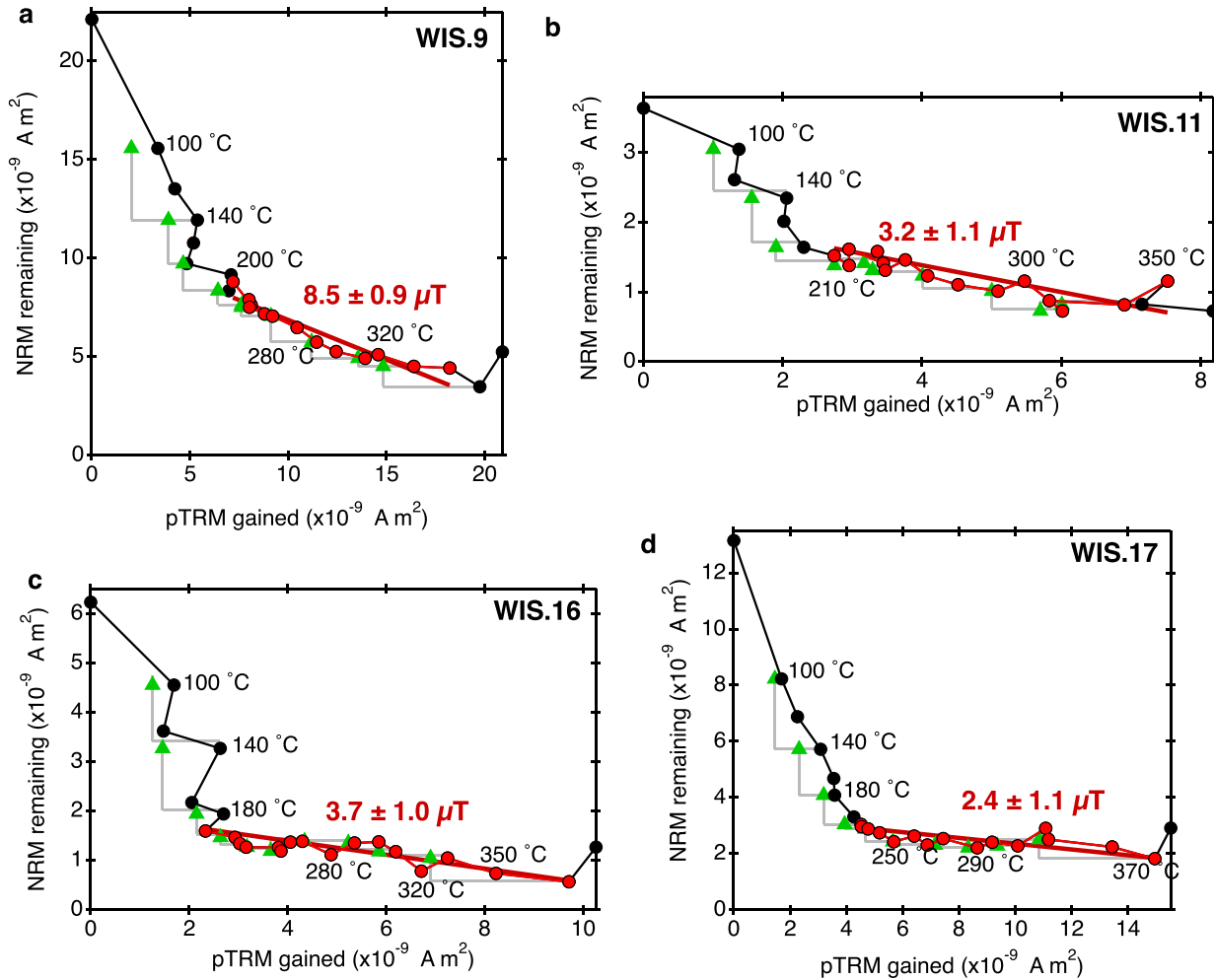


**Figure 8.** Double heating paleointensity analyses of WIS 9160. The NRM remaining in each sample is plotted against its pTRM gained during the double heating measurements (Arai diagram) measured for all four subsamples with low DRATS values and did not display visibly poor Arai diagrams. The HT component is depicted by the red points, and the recovered paleointensity from each subsample is denoted by the red least-squares fit line and the red text. The temperature corresponding to some of the heating steps points during thermal demagnetization is shown by the black text. The pTRM checks are shown by the green triangles, and the preceding thermal step is depicted by the gray lines.

the structure of the organic matter in WIS 91600 is consistent with short-lived and relatively mild heating on its parent body (Quirico et al. 2018). Finally, our thermal and AF demagnetization measurements also constrain the peak metamorphic temperature of this meteorite to between 400°C and 500°C (Sections 2.3 and 2.4).

The cooling timescale of WIS 91600 can be constrained by the length scale of Fe–Ni sulfide microstructures in this meteorite. WIS 91600 contains large ( $\sim 50 \mu\text{m}$ ) matrix-hosted pyrrhotite grains that contain numerous dispersed blebs of pentlandite (Figure 9). These Fe–Ni sulfides form a solid solution at temperatures  $\geq 400^\circ\text{C}$  that breaks down to form this microstructure on cooling from  $\sim 400^\circ\text{C}$  to  $200^\circ\text{C}$  (Kelly & Vaughan 1983; Kimura et al. 2011). As such, this microstructure is characteristic of meteorites that have been mildly heated (to  $\geq 400^\circ\text{C}$ ) on their parent asteroids (Kimura et al. 2011). The size of the pentlandite blebs increases with cooling time over a period of hours to days (Kelly & Vaughan 1983). The width of pentlandite blebs in WIS 91600 is typically  $\lesssim 4 \mu\text{m}$  (Figure 9), which is smaller than those in controlled laboratory samples heated to  $400^\circ\text{C}$  for 10 hr ( $\gtrsim 7 \mu\text{m}$ ; Kelly & Vaughan 1983). As such, WIS 91600 appears to have cooled to  $200^\circ\text{C}$  faster than this time period (likely over 1–10 hr). This cooling could have occurred either by radiation if WIS 91600 was at the surface of its parent body or by conduction to

neighboring clasts if it was buried in a cold regolith following heating.

This peak temperature and cooling timescale, as well as the structure and composition of IOM (Yabuta et al. 2010; Quirico et al. 2018) and infrared spectra (Beck et al. 2014a), argue that WIS 91600 was heated by an impact. The timing of this impact heating in WIS 91600 has not been measured. However, the timing of impacts onto the parent bodies of other aqueously altered chondrites has been constrained by examining their microstructures. For example, petrofabrics and foliation in CM (Rubin 2012), CR (Renazzo-like; Rubin & Harju 2012), CV (Vigarano-like; Forman et al. 2017), and other carbonaceous chondrites (Gattacceca et al. 2005) have been used to argue that the parent bodies of these meteorites experienced multiple low-energy impacts during their early histories. These impacts were too weak to alter the bulk shock stage of these meteorites, but they have been proposed to have affected the matrices of these meteorites on micrometer length scales. Furthermore, these impacts have been proposed to have facilitated the aqueous alteration of these meteorites (Hanna et al. 2015; Lindgren et al. 2015), suggesting they occurred within the first  $\sim 5$  Myr following CAI formation (Doyle et al. 2015; Jilly-Rehak et al. 2017). These impacts are also thought to have imparted small

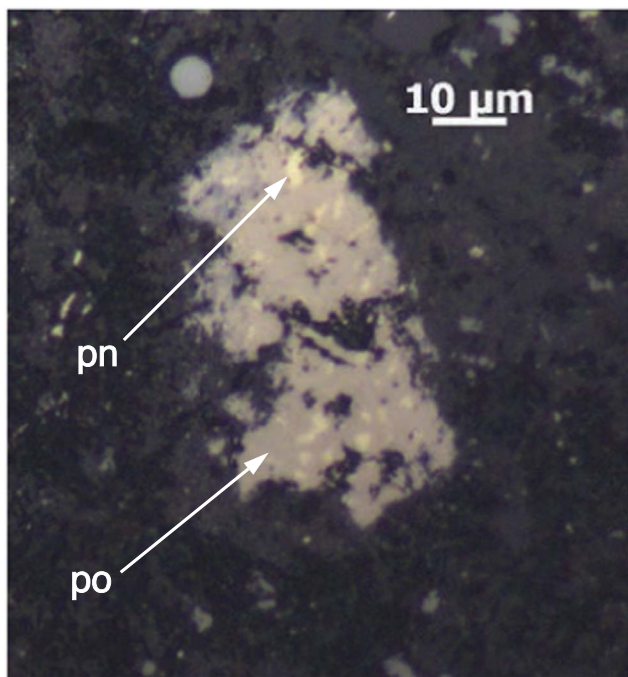


**Figure 9.** Reflected light microscope image of a pyrrhotite (po) grain containing blebs of pentlandite (pn) in WIS 91600. These blebs form on cooling from  $\sim 400^\circ\text{C}$  and are typically  $< 4 \mu\text{m}$ .

amounts of heat to these chondrites. The recovered precipitation temperatures of type 2 calcites in “unheated” CM chondrites is  $< 130^\circ\text{C}$ – $200^\circ\text{C}$  (Chan et al. 2017; Verdier-Paoletti et al. 2017; Vacher et al. 2018), suggesting these impacts could possibly have heated these meteorites by a few tens of degrees to possibly  $100^\circ\text{C}$ . Some CM (Tonui et al. 2014), CI-like (King et al. 2015), CR (Briani et al. 2013), and C2 (Quirico et al. 2018) chondrites, including WIS 91600 (Yabuta et al. 2010), were heated to significantly higher temperatures on their parent bodies ( $300^\circ\text{C}$ – $900^\circ\text{C}$ ), also likely by impacts. The partially dehydrated nature of these heated meteorites indicates that this higher-temperature heating occurred after or near the end of the main stage of aqueous alteration (Nakamura 2005). As such, it is feasible that “unheated” and some heated chondrites could have been metamorphosed by the same stream of early, low-energy impacts, and that the heated meteorites reached higher peak metamorphic temperatures because they originate from closer to the point of one of these impacts (Chan et al. 2017; Vacher et al. 2018). Constraints on the possible timing of this impact heating can be recovered from the age of type 2 calcites in these meteorites, which are thought to have formed at elevated temperatures (Chan et al. 2017; Verdier-Paoletti et al. 2017; Vacher et al. 2018). These calcites were one of the last phases to form during aqueous alteration of “unheated” CM chondrites (Lee et al. 2014), suggesting that these meteorites were weakly heated during the later stages of aqueous alteration. The measured Mn–Cr ages of carbonates in “unheated” CM, CI, and C2 chondrites all fall within the errors of each other between  $\sim 3.6$  and  $5.0$  Myr after CAI formation, further suggesting that weak heating occurred during the aqueous alteration of these meteorites (Fujiya et al. 2012, 2013; Jilly et al. 2014; Doyle et al. 2015). The carbonate ages recovered from the heated CI-like chondrite Yamato 980115 (peak

metamorphic temperature  $> 500^\circ\text{C}$ ; King et al. 2015) and the impact-heated CM2.0/2.1 chondrite Sutter’s Mill (some stones reached peak metamorphic temperature  $> 500^\circ\text{C}$ ; Jenniskens et al. 2012; Beck et al. 2014b; Quirico et al. 2018) both fall at the older end of this range ( $\sim 3.6$ – $3.7$  Myr after CAI formation; Fujiya et al. 2013; Jilly et al. 2014), suggesting that the impacts that more strongly heated some CM, CI-like, and C2 chondrites can have occurred during or at the end of the main phase of aqueous alteration. Moreover, Fujiya et al. (2015) note that Mn–Cr dating does not currently have the analytical precision to resolve the formation ages of early, pore-filling, low-temperature type 1 calcites and later, high-temperature type 2 calcites that replace other minerals, further supporting near-concurrent low- and high-temperature carbonate growth between  $\sim 3.6$  and  $5.0$  Myr after CAI formation in these meteorites. Finally, the presence of anhydrous minerals in WIS 91600 suggests either that heating happened late enough during the sequence of aqueous alteration that these phases were not rehydrated, or that heating potentially occurred earlier during aqueous alteration and this event caused some water to be lost from this meteorite, preventing complete rehydration (Nakamura 2005).

Together, all of these observations argue that aqueously altered chondrites can have been heated by a stream of low-energy impacts during the later stages of aqueous alteration ( $\sim 3$ – $5$  Myr after CAI formation), and that these impacts caused localized regions of the parent asteroids of these meteorites to have reached relatively high temperatures. As such, impact heating could have overlapped with the later stages of the solar nebula (which likely persisted until sometime between  $3.7$  and  $3.8$ – $4.8$  Myr after CAI formation; Wang et al. 2017; Schrader et al. 2018; Fu et al. 2020). Hence, it is possible that WIS 91600 was impact heated during the later stages of the solar nebula. In this case, we expect that WIS 91600 would have recorded a pTRM of the nebula field (Figure 11).

Due to thermal re-equilibration between their cores and mantles following differentiation, asteroids are not expected to have generated magnetic fields through core dynamo activity until  $\gtrsim 5$  Myr after CAI formation (Bryson et al. 2019a). Specifically for an asteroid composed of high-porosity CM/CI/C2-like material, dynamo activity is predicted to be delayed until  $\gtrsim 5.5$  Myr after CAI formation. This delay in dynamo activity is corroborated by the weak paleointensities ( $\lesssim 0.6 \mu\text{T}$ ) recovered from the volcanic angrites (recorded at  $\sim 3.8$ – $4.8$  Myr after CAI formation; Wang et al. 2017) and the CRM carried by the Kaba CV chondrite (recorded sometime between  $\sim 4$  and  $6$  Myr after CAI formation; Gattacceca et al. 2016). As such, if WIS 91600 was impact heated during the lifetime of the nebula, it is very unlikely that this meteorite would have also experienced a dynamo field at this time if its parent body was partially differentiated and large enough to have generated a dynamo field (Figure 11). If WIS 91600 was impact heated  $\gtrsim 5.5$  Myr after CAI formation, it is feasible that this meteorite could have recorded a pTRM of a field created by internal core dynamo activity if the WIS 91600 parent body was partially differentiated and large enough to have generated a dynamo field. Including both thermally and compositionally driven dynamo activity, these fields could have been generated (possibly intermittently) until  $\sim 10$ – $700$  Myr after CAI formation depending on the radius of the parent body up to  $500$  km (Bryson et al. 2019a). However, one- and two-stage accretion models that produce partially differentiated bodies involve

chondritic material in direct contact with the hot interior of a body, causing the base of this chondritic material to be heated by several hundreds of degrees over long periods (millions of years; Lichtenberg et al. 2018; Bryson et al. 2019a). As there is no evidence of such prolonged high-temperature heating in any extensively aqueously altered chondrite, there is no evidence that the parent bodies of these meteorites were partially differentiated. This differs from the CV, H (high-metal ordinary chondrites), and R (Rumuruti-like) chondrites, the parent bodies of which have been suggested to have been partially differentiated (Carporzen et al. 2011; Bryson et al. 2019b; Cournede et al. 2020), and all have members that were heated to high temperatures on their parent bodies for extended time periods (almost certainly  $\gtrsim 500^\circ\text{C}$ ; Bonal et al. 2016; and possibly  $\sim 900^\circ\text{C}$  if the CV and CK chondrites originate from the same parent body; Greenwood et al. 2010). As such, we disfavor core dynamo activity as the origin of the remanence we measured in WIS 91600.

It has recently been argued that the intensity of the field supported by the solar wind was  $< 0.1 \mu\text{T}$  in the terrestrial planet formation region of the solar system and would have been minimally amplified (by a factor of  $< 3.5$  times) by pile up ahead of an asteroid-sized body (Oran et al. 2018). The weak intensity of the solar wind field in this region of the solar system is also corroborated by the remanence carried by the volcanic angrites (paleointensity  $\lesssim 0.6 \mu\text{T}$ ; Wang et al. 2017) and the CRM carried by the Kaba CV chondrite (paleointensity  $\lesssim 0.3 \mu\text{T}$ ; Gattacceca et al. 2016). The solar wind field is, therefore, too weak by at least an order of magnitude to explain the paleointensity we recover from WIS 91600, indicating that it was not the main source of the remanence in this meteorite (Figure 11).

Transient magnetic fields have been proposed to have been generated by large impacts onto asteroid-sized bodies (i.e., those that produced craters a few hundred kilometers in diameter). These fields are calculated to have lasted  $< 10\text{--}100$  s (Crawford & Schultz 1999, 2000). The timescale of cooling over different temperature intervals within a carbonaceous chondrite following impact heating can be constrained by thermal modeling. Low-energy impacts into carbonaceous chondrite material are predicted to have introduced pressure waves that caused micropore compaction in the matrix of these meteorites, which generated heat in this component (Bland et al. 2014). Inclusions such as chondrules were originally far less porous than the matrix and so are predicted to have been significantly less heated by these pressure waves. Models of this process indicate that impact velocities of  $\sim 1.2\text{--}1.4 \text{ km s}^{-1}$  produced peak matrix and chondrule temperatures of  $400^\circ\text{C}\text{--}500^\circ\text{C}$  and  $\sim 25^\circ\text{C}\text{--}50^\circ\text{C}$ , respectively, within tens of microseconds of the pressure wave moving through a chondrite that is composed of a 70:30 mixture of matrix:chondrules (Bland et al. 2014). As such, WIS 91600 likely contained significant temperature variations over micrometer to millimeter length scales shortly after it was heated. Immediately following its production in the matrix, this heat will have diffused into the cold chondrules, causing the temperature of both the chondrules and matrix to evolve toward an average re-equilibrated value. We constrained this re-equilibrated temperature as well as the timescale over which it was reached by performing thermal conduction models of a chondrite immediately after its matrix had been heated by an impact pressure wave. These models consisted of a two-dimensional distribution of chondrules embedded in matrix. The sizes of the chondrules were distributed

around the measured mean value in WIS 91600 ( $400 \mu\text{m}$ ; Choe et al. 2010) and were present at the measured abundance of chondrules and other mineral fragments in WIS 91600 (15 vol%; Birjukov & Ulyanov 1996). At the initial time step, the temperature of the chondrules was set to  $25^\circ\text{C}$ , and the temperature of the matrix was set uniformly to  $450^\circ\text{C}$ , mimicking the expected thermal state of WIS 91600 shortly after impact heating (Figure 10(a)). We then solved the two-dimensional heat conduction equation

$$\frac{\partial T}{\partial t} = \kappa \left( \frac{\partial^2 T}{\partial x^2} + \frac{\partial^2 T}{\partial y^2} \right) \quad (4)$$

where  $T$  is temperature,  $t$  is time,  $\kappa$  is thermal diffusivity, and  $x$  and  $y$  are the dimensional coordinates. We solved this equation iteratively with a time step of 0.1 ms over a total time of 2 s, a cell size of  $20 \mu\text{m}$ , and a thermal diffusivity in the matrix of  $4 \times 10^{-7} \text{ m}^2 \text{ s}^{-1}$  and in the chondrules of  $8 \times 10^{-7} \text{ m}^2 \text{ s}^{-1}$  (Opeil et al. 2012) using period boundary conditions. The results of this model demonstrate that both chondrules and the matrix reached a re-equilibrated temperature of  $\sim 415^\circ\text{C}$  in  $< 2$  s (Figure 10). In reality, conduction will have occurred in three dimensions, which will have caused this temperature to have been reached in a slightly shorter time. Both components will then have cooled together, which, as discussed earlier in this Section, likely took 1–10 hr (to cool to  $\sim 200^\circ\text{C}$ ). This result indicates that grains with blocking temperatures  $\gtrsim 415^\circ\text{C}$  could have cooled within the lifetime of an impact-generated field (Figure 10). As such, these grains could have recorded a remanence of this field if the impact that heated WIS 91600 was large enough to have generated such a field and there was minimal plasma dissipation. However, our HT paleointensities are recovered from the remanence recorded on cooling from  $\leq 370^\circ\text{C}$  (Figure 10(f)). Grains with these blocking temperatures cooled much more slowly (period of hours) after the rapid thermal re-equilibration following impact heating and so are not expected to have cooled within the lifetime of an impact-generated field. It is, therefore, extremely unlikely that the HT remanence we measured was imparted by an impact-generated field (Figure 11).

The post-impact, thermally re-equilibrated temperature of WIS 91600 will have been lower if the matrix was only heated to  $400^\circ\text{C}$  by the impact pressure wave. Although such a low temperature is unlikely based on the concentration of thermally labile elements in WIS 91600 (Tonui et al. 2014), grains with blocking temperatures at the higher end of our HT range could have cooled quickly enough to have recorded an impact-generated field in this case. However, the paleodirections and paleointensities recovered from different temperature intervals within our HT range are unidirectional (Figure 4), indicating that all of the grains across the HT range recorded the same field direction and intensity during the whole period of cooling down to  $\sim 200^\circ\text{C}$ . As grains with lower blocking temperature in this range certainly could not have cooled quickly enough to have recorded an impact-generated field, this observation suggests that our HT remanence does not contain a vestige of any such fields. Similarly, the thermally re-equilibrated temperature of WIS 91600 will have been higher if the matrix reached  $500^\circ\text{C}$ . In this case, it becomes even less likely that the HT remanence could have been imparted by an impact-generated field because

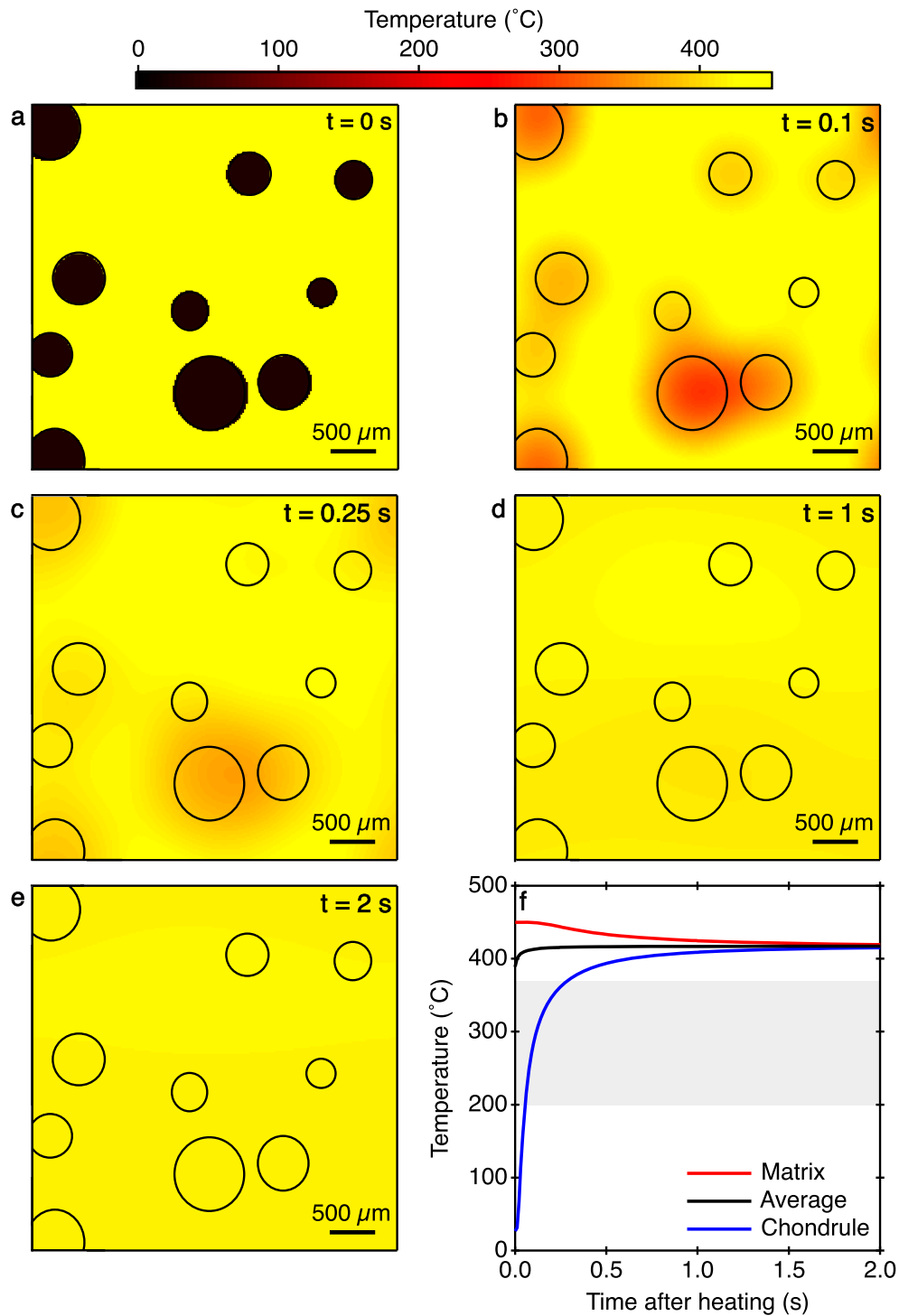


**Figure 10.** Results of our thermal evolution modeling of a chondrite immediately following matrix heating by the passage of an impact pressure wave through the sample. (a) Initial thermal state consisting of cold ( $25^{\circ}\text{C}$ ) chondrules and heated ( $450^{\circ}\text{C}$ ) matrix. The size distribution and abundance of chondrules match those observed experimentally for WIS 91600 (Birjukov & Ulyanov 1996; Choe et al. 2010). (b)–(e) Thermal state of the chondrite at 0.1 s, 0.25 s, 1 s, and 2 s, respectively, after heating. The whole assemblage has reached a near-isothermal state by 2 s after heating. (f) The calculated thermal evolution of the center of the largest chondrule, the center of the largest area of matrix, and the average of the whole assemblage. The matrix cools from  $450^{\circ}\text{C}$  to  $\sim 415^{\circ}\text{C}$  and the chondrules heat up from  $25^{\circ}\text{C}$  to  $\sim 415^{\circ}\text{C}$  in  $< 2$  s. The temperature range over which we recovered our HT paleointensity is depicted by the gray bar. None of the material in our model cools through this temperature range within the first 2 s following heating.

the thermally re-equilibrated temperature is further from our HT range.

The cooling timescale and possible impact age of WIS 91600 permit this meteorite to have recorded a snapshot of the instantaneous component of the nebula field (Figure 11). As we

are able to disfavor or rule out other potential field sources, we ascribe the HT remanence we measure to this field. This scenario has been proposed previously for other carbonaceous chondrites (Cournede et al. 2015; Muxworthy et al. 2017), and our recovered paleointensities agree with MHD model

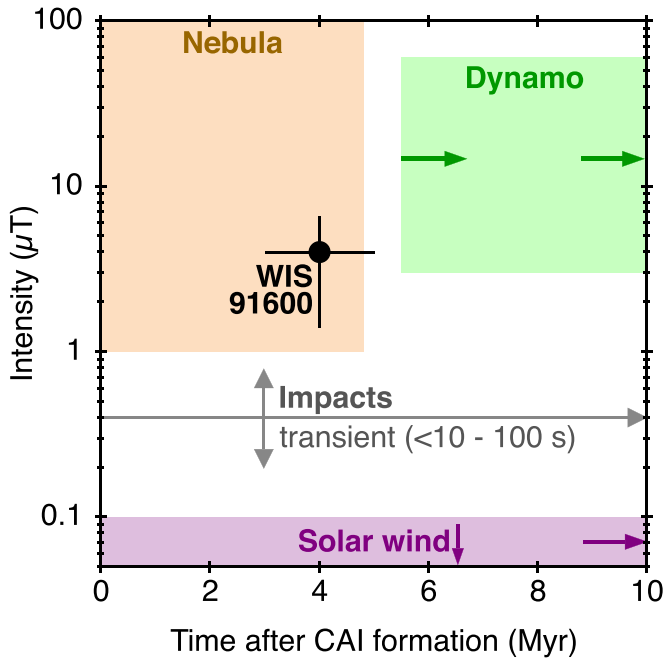


**Figure 11.** The timings and predicted intensities of different fields that could potentially have imparted remanences to chondrites in the first 10 Myr of the solar system. The solar wind field (purple) is  $<0.1 \mu\text{T}$  and continued after 10 Myr after CAI formation (purple arrow; Oran et al. 2018). Dynamo activity (green) is delayed until  $>5.5$  Myr after CAI formation in a partially differentiated C2-like asteroid (Bryson et al. 2019a) and could have continued after 10 Myr after CAI formation (green arrow). The range of possible paleointensities encompasses the values recovered from paleomagnetic measurements of a number of CV chondrites (Carporzen et al. 2011; Gattacceca et al. 2016). Impacts (gray) are sporadic and could feasibly occur at any time during the early solar system and produce transient fields (lasting  $<10$ – $100$  s; Crawford & Schultz 1999, 2000). The intensity of these fields depends strongly on the distance of the meteorite from the point of impact and the energy of the impact. The nebula field (orange) persisted until sometime between  $\sim 3.7$  and  $\sim 3.8$ – $4.8$  Myr after CAI formation (Wang et al. 2017; Schrader et al. 2018; Fu et al. 2020), and the calculated intensity of the instantaneous component ranges between  $\sim 1$  and  $100 \mu\text{T}$  with heliocentric distance in the solar nebula (Bai & Goodman 2009, Figure 12). The possible impact age of WIS 91600 (recovered from the measured precipitation ages of type 2 calcites in heated and unheated CM, CI, and C2 chondrites; Fujiya et al. 2012, 2013; Jilly et al. 2014) and our recovered average HT paleointensity are included as the black point. This intensity, timing, and duration of remanence acquisition are consistent with the nebula field as the source of the remanence in this meteorite.

predictions of this field (Bai & Goodman 2009, see Section 4.2). This scenario would require that WIS 91600 was impact heated within the lifetime of the nebula.

The time-averaged magnetic field experienced by material that is rotating quickly compared to its timescale of remanence acquisition corresponds to the projection of the field onto its rotation axis. The intensity of this projected field depends on the angle of the spin axis. Assuming the orientation of the spin axis could have been distributed uniformly over a hemisphere, the average intensity of the projected field would have been half that of the background field (Fu et al. 2014). Examples of materials that recorded such time-averaged, projected fields include individual chondrules (Fu et al. 2014, 2020), bulk CM chondrites (Cournede et al. 2015), and Tagish Lake (Bryson et al. 2020). Consequently, the paleointensities recovered from these samples were multiplied by the average factor of two to recover the intensity of the background nebula field. However, because WIS 91600 cooled over a few hours, it is possible that its parent body underwent minimal rotation while this meteorite

recorded its pTRM. Hence, we did not correct our recovered paleointensity by this factor. This treatment is supported by the unidirectional remanence we measure across the HT and HC components in our subsamples of WIS 91600 (Figure 4), which indicate that the orientation of this meteorite and the magnetic field it recorded did not vary as this meteorite cooled.

#### 4.2. The Formation Distance of the WIS 91600 Parent Body

Our recovered HT double heating paleointensity from WIS 91600 is  $4.4 \pm 2.8 \mu\text{T}$  ( $1\sigma$ ). Given the thermal history of WIS 91600 and the minimal alteration caused by our thermal demagnetization measurements, this value does not share the same uncertainties as that recovered from Tagish Lake (i.e., associated with the recording efficiencies of CRMs and the recovery of thermal-equivalent paleointensities from ARM and IRM methods; Bryson et al. 2020). The various and significant uncertainties associated with our ARM and IRM paleointensity values make these considerably less reliable estimates of the paleointensity of the field experienced by WIS 91600. We wish to simply state that our ARM and IRM paleointensity values are consistent with the double heating paleointensity values that we calculated. We report these ARM and IRM paleointensity values in the interest of completeness and to demonstrate consistency rather than to use them as reliable values of the paleointensity experienced by WIS 91600. Instead, we focus on our recovered HT double heating paleointensity value, as this value is considerably more reliable.

A quantitative estimate of the formation distance of the WIS 91600 parent body can be recovered by comparing our HT double heating paleointensity value to MHD model predictions of the intensity of the instantaneous component of the nebula field. These MHD models currently predict minimum possible intensity estimates that produced a given steady-state solar accretion rate for a given mechanism of angular momentum transfer in the disk (Bai & Goodman 2009). The absolute intensities predicted by these models currently contain a number of uncertainties. However, these models do provide the expected functional form of the decay of the intensity of this field with distance from the Sun ( $B_{\text{neb}} \propto x^{-\frac{11}{8}}$  and  $B_{\text{neb}} \propto x^{-\frac{5}{4}}$  for radial-azimuthal [ $r\phi$ ] and vertical-azimuthal [ $z\phi$ ] coupling of the Maxwell stress tensor, respectively, where  $B_{\text{neb}}$  is the intensity of the instantaneous component of the nebula field and  $x$  is heliocentric distance). It is possible to constrain the intensity profiles calculated from these models using paleointensities recovered from meteorites. This process produces profiles that represent the paleointensities that would have been recorded by different meteorites during the lifetime of the nebula. Importantly, the paleointensity recovered from a meteorite depends on the mechanism by which it was imparted. Also, the intensity of the nebula field could have varied with time until it decayed entirely when the nebula dissipated. Finally, the timescale over which the field was recorded likely also affected the paleointensity experienced by a meteorite. As such, a number of different constrained intensity profiles can be produced that each correspond to the expected intensity that would have been recorded during different remanence acquisition mechanisms, times, and durations. Given the quick cooling of WIS 91600 possibly at  $\sim 3$ – $5$  Myr after CAI formation, we chose to constrain the nebula field profile using the paleointensities recovered from individual chondrules (Fu et al. 2014, 2020). These spherules recorded remanences through the same mechanism, at a similar time (between  $\sim 2$

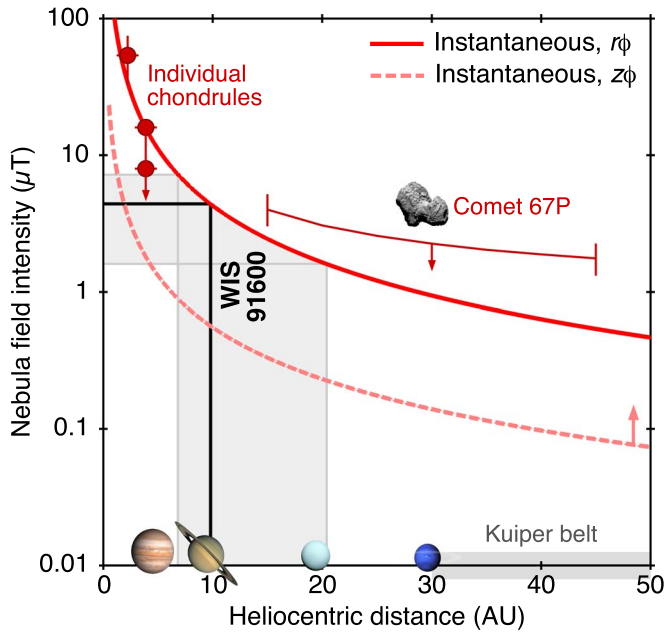


**Figure 12.** Calculated minimum intensity profiles of the instantaneous component of the nebula field for vertical-azimuthal ( $z\phi$ ) and radial-azimuthal ( $r\phi$ ) coupling of the Maxwell stress tensor required to generate a steady-state solar accretion rate of  $10^{-8} M_{\text{Sun}} \text{Myr}^{-1}$  (Bai & Goodman 2009). The paleointensities recovered from individual chondrules extracted from an LL chondrite (Fu et al. 2014), the upper limits on the possible paleointensities experienced by individual chondrules extracted from two CR chondrites (Fu et al. 2020), and the paleointensity limit recovered from comet 67P/Churyumov–Gerasimenko during the Rosetta mission (Biersteker et al. 2019) are plotted at estimates of their formation distances (Desch et al. 2018). The calculated minimum intensity estimate for  $r\phi$  coupling is consistent with the measured paleointensities of the individual chondrules and the limit recovered from 67P/Churyumov–Gerasimenko. As such, for the purposes of this study, we assume that this minimum intensity profile represents the paleointensities that would be recorded by quickly cooled meteorites during the later stages of the solar nebula (matching the possible thermal history of WIS 91600). Because the calculated profiles are minimum intensity estimates, the calculated profile for  $z\phi$  coupling is still compatible with the measured paleointensities from the individual chondrules. However, the recovered paleointensities argue that, if this was the form of the coupling of the Maxwell stress tensor, this field must have been approximately an order of magnitude stronger than its minimum possible value. If this were the case, the profile for  $z\phi$  coupling would produce a very similar estimate of the formation distance of the WIS 91600 parent body to that predicted by our adopted  $r\phi$  profile. The adopted intensity profile reaches  $4.4 \mu\text{T}$  at 9.8 au (black lines), indicating that WIS 91600 was impact heated in the far reaches of the solar system. The ranges of uncertainty in the paleointensity (accounting for the range in our values recovered from individual subsamples) and formation distances are shown by the gray bars. The present-day heliocentric distances of the giant planets and Kuiper Belt are included.

and 4 Myr after CAI formation; Kruijjer et al. 2019) and over a similar duration (period of hours) as WIS 91600. The paleointensity recovered from WIS 91600 is approximately an order of magnitude weaker than that recovered from chondrules extracted from an LL chondrite ( $54 \pm 21 \mu\text{T}$ ; Fu et al. 2014), immediately suggesting that WIS 91600 formed at a larger heliocentric distance than that of the LL chondrite parent body (i.e.,  $\gtrsim 2\text{--}3$ ; Desch et al. 2018). The predicted minimum nebula field intensity for  $r\phi$  coupling of the Maxwell stress tensor and a solar accretion rate of  $10^{-8} M_{\text{Sun}} \text{Myr}^{-1}$  (which matches the average rate measured from other sunlike stars during their disk phases; Hartmann et al. 1998) matches the measured paleointensities of these chondrules at independent estimates of their formation distances (Desch et al. 2018; Figure 12). This intensity profile is also broadly consistent with

the paleointensity limit recovered from the magnetic measurements of comet 67P/Churyumov–Gerasimenko made during the Rosetta mission (Biersteker et al. 2019) and the paleointensity limits recovered from individual chondrules extracted from two CR chondrites (Fu et al. 2020). As such, we assume for the purpose of this study that the minimum intensity profile calculated using these parameters represents the intensity profile that would have been recorded by meteorites that cooled quickly during the later stages of the solar nebula. It is worth noting that the field profiles predicted by these MHD models remain uncertain, the solar accretion rate is poorly constrained by independent observations, and the mechanism of angular momentum transfer in the disk is unknown. However, our adopted intensity profile is supported by the paleointensities recovered from individual chondrules and the average accretion rate of other sunlike stars.

This constrained profile reaches an intensity of  $4.4 \mu\text{T}$  at a heliocentric distance of 9.8 au (Figure 12), arguing that the WIS 91600 parent body recorded its NRM in the far reaches of our solar system at a significantly larger heliocentric distance than that proposed for most other meteorite parent bodies (Desch et al. 2018). The most straightforward mechanism explaining how this body was found at this large heliocentric distance is that it formed there, arguing that the parent bodies of some meteorites formed in the distal solar system. The uncertainty in our recovered average HT paleointensity corresponds to formation distances between 6.8 and 20.4 au. This observation places the formation of the WIS 91600 parent body at a similar distance to the lower end of the recovered range of possible formation distances of the Tagish Lake parent body ( $>8\text{--}13$  au; Bryson et al. 2020). This distance is beyond the formation distances of the giant planets in the pre-migrational planetary arrangement proposed by the Grand Tack model (Walsh et al. 2011). Many of the bodies that formed at a similar distance as the WIS 91600 parent body are predicted to have been outwardly scattered by the migration and/or growth of the giant planets in this model and are predicted to constitute a significant fraction of the present-day Kuiper Belt (DeMeo & Carry 2014). This observations suggests that some larger Kuiper Belt objects may have similar compositions and petrologies to WIS 91600.

If WIS 91600 had formed at a similar heliocentric distance as the CM chondrite parent body ( $\sim 3.75$  au; Desch et al. 2018), we expect it would have recorded a similar CRM as it underwent aqueous alteration prior to impact heating to that measured in Murchison (i.e., blocked up to  $580^\circ\text{C}$  and corresponding to a paleointensity of  $\sim 1\text{--}2 \mu\text{T}$ ; Cournede et al. 2015). This remanence would have been preserved in WIS 91600 by grains with blocking temperatures greater than its peak metamorphic temperature (i.e.,  $>400^\circ\text{C}\text{--}500^\circ\text{C}$ ). The remanence remaining in our subsamples after heating to the end of the HT range is weak and broadly similarly oriented to the HC and HT components (Figure 4, Tables 2 and 4), suggesting that this remanence is dominated by the remaining pTRM carried by grains with blocking temperatures greater than the end of the HT range ( $>390^\circ\text{C}$ ) and not a CRM carried to  $580^\circ\text{C}$ . As such, WIS 91600 does not appear to carry a similar CRM to that carried by the CM chondrites. This observation suggests that the intensity of the time-averaged stable component of the nebula field experienced by this meteorite during aqueous alteration was weaker than that experienced by the CM chondrites (i.e.,  $<2 \mu\text{T}$ ). Although the pTRM overprint

and significant alteration during our thermal demagnetization measurements at temperatures  $>390^{\circ}\text{C}$  make the paleointensity of this CRM carried by WIS 91600 difficult to quantify reliably, the absence of a clear CRM at temperatures greater than the peak metamorphic temperature supports the distal formation of the WIS 91600 parent body (Bryson et al. 2020), certainly at a greater heliocentric distance than that of the CM chondrite parent body.

Moreover, this recovered weak stable component intensity suggests that WIS 91600 would have experienced a weak crustal remanent field as it cooled. Following the analysis of Fu et al. (2012), an estimate of the intensity of this crustal remanent field can be calculated from our IRM measurements of WIS 91600. The average saturation remanent magnetization of WIS 91600 recovered from all five of our AF subsamples is  $\sim 0.6 \text{ A m}^2 \text{ kg}^{-1}$ , and the lack of a clear CRM at temperatures  $>390^{\circ}\text{C}$  suggests that a crustal remanence was imparted by a field with an intensity that is certainly  $<2 \mu\text{T}$ . These values produce a range of possible expected CRMs of  $<0.4 \text{ mA m}^2 \text{ kg}^{-1}$ . For a density of WIS 91600 of  $2100 \text{ kg m}^{-3}$  (the average value of CM and CI chondrites; Elkins-Tanton et al. 2011), these values indicate that the crustal remanent field experienced by WIS 91600 would have been  $<0.7 \mu\text{T}$ , which is a factor of  $>5.5$  times weaker than the average double heating paleointensity we recovered. As such, we disfavor a crustal remanent field as the origin of the pTRM carried by WIS 91600.

#### 4.3. Constraints on the Migration of Kilometer-sized Bodies

The pre-impact orbit of a meteorite can be calculated from its fall if this event is sufficiently well documented. All meteorites from which reliable orbital parameters have been recovered came to Earth from the asteroid belt (Granvik & Brown 2018). It is, therefore, reasonable to assume that WIS 91600 also came to Earth from the asteroid belt. Combined with our recovered formation distance, this observation argues that the WIS 91600 parent body previously migrated from  $\sim 10$  au to 2–3 au. Our results, therefore, support the transport of asteroid-sized bodies throughout the solar system and provide a quantitative estimate of the region of the solar system from which these bodies could have been making their way to the asteroid belt. Such migrations have been previously proposed by models of orbital dynamics (Levison et al. 2009) and supported by measurements of meteorites (Kruijer et al. 2019; Bryson et al. 2020). The migrations of small planetary bodies are thought to have populated the asteroid belt (Raymond & Izidoro 2017), formed the Kuiper Belt (DeMeo & Carry 2014), and potentially delivered water-rich bodies to the inner solar system (Gomes et al. 2005). The only processes that have been proposed to have caused small bodies to have migrated throughout the solar system are the growth and/or migrations of the giant planets (Raymond & Izidoro 2017; Nesvorný 2018). Hence, our results also favor the giant planets having played key roles in establishing the large-scale architecture of the solar system (Walsh et al. 2011). We are unable to constrain the timing of the inward transport of the WIS 91600 parent body or the specific mechanism that drove the motion of this body from our observations.

#### 4.4. Constraints on the Migration of Millimeter-sized Solids

WIS 91600 contains chondrules (mean size  $400 \mu\text{m}$ , largest size  $\gtrsim 1000 \mu\text{m}$ ), amoeboid olivine aggregates (AOAs;  $300\text{--}450 \mu\text{m}$ ), and CAIs (Choe et al. 2010; Yamanobe et al. 2018). Combined

with our recovered formation distance, this observation indicates that large, thermally processed solids were present at  $\sim 10$  au by  $\sim 3\text{--}4$  Myr after CAI formation (the likely accretion age of the WIS 91600 parent body, see Section 1). This observation is supported by the presence of chondrules, AOAs, and CAIs in Tagish Lake (Bryson et al. 2020) and the material collected from the coma of comet 81P/Wild2 during the Stardust mission (Brownlee et al. 2006). The average oxygen isotopic composition of type I chondrules in WIS 91600 (Yamanobe et al. 2018) and Tagish Lake (Russell et al. 2010) are within the error of those in CO (Ormans-like; Tenner et al. 2013) and CM chondrites (Chaumard et al. 2018; Figure 13). This observation suggests that the chondrules in Tagish lake and WIS 91600 formed from the same reservoir as the CO and CM chondrules, which likely existed around the formation distance of the CO and CM chondrite parent bodies ( $\sim 3.75$  au; Desch et al. 2018). Al–Mg dating demonstrates that the CO chondrules formed  $\sim 2.5$  Myr after CAI formation (Kruahashi et al. 2008). Based on measured carbonate formation ages, the CM parent body has been calculated to have accreted sometime between 3.0 and 3.5 Myr after CAI formation (Fujiya et al. 2012), indicating that the chondrules in this group must have formed before this time (likely  $\lesssim 0.2$  Myr before parent body accretion; Alexander 2005). Assuming that chondrules in WIS 91600 and Tagish Lake formed within the same period as those in the CO and CM chondrites (i.e.,  $\sim 2.5\text{--}3.5$  Myr after CAI formation), our observation indicates that large, thermally processed solids traveled outward from  $\sim 3\text{--}4$  au to  $\sim 10$  au within  $0.5\text{--}1.0$  Myr of their formation, suggesting that some chondrules traveled very quickly in the solar nebula (average speed of  $\gtrsim 7$  au  $\text{Myr}^{-1}$ ). If the chondrules in WIS 91600 and Tagish Lake formed earlier than those in the CO and CM chondrites, they could have reached the far reaches of the solar system at slower average migration speeds. CAIs and AOAs are thought to have formed at  $<1$  au from the Sun and are the oldest solids that formed in the solar system (Scott & Krot 2014). Their presence in WIS 91600 indicates that some CAIs traveled from the innermost solar system to the far reaches of the solar system with an average speed of  $\gtrsim 3$  au  $\text{Myr}^{-1}$ .

#### 4.5. Constraints on the Migration of Micrometer-sized Material and Ice

The oxygen isotopic composition of bulk samples of WIS 91600, Tagish Lake, and the CI chondrites (proposed to originate from  $>15$  au based on their refractory concentration and CAI abundance; Desch et al. 2018) fall between  $\delta^{18}\text{O} = 15\text{--}20 \text{ ‰}$  and  $\delta^{17}\text{O} = 8\text{--}10 \text{ ‰}$  (Rowe et al. 1994; Clayton & Mayeda 1999; Brown et al. 2000; Choe et al. 2010; Herd et al. 2012; Tonui et al. 2014; Figure 13). These meteorites are typically matrix-rich (can contain  $\gtrsim 80\text{--}95 \text{ vol}\%$  matrix; Birjukov & Ulyanov 1996; Zolensky et al. 2002; Scott & Krot 2014), so these values are very likely dominated by the oxygen isotopic composition of the matrices of these meteorites. These values are distinct from those measured in most other bulk meteorites (Clayton 2003; thought to form at heliocentric distances between  $\sim 2$  and 4 au; Desch et al. 2018) as well as the primitive chondritic mineral (PCM; Ushikubo et al. 2012) and carbonaceous chondrite anhydrous mineral (CCAM; Clayton & Mayeda 1999) lines that track the evolution of the oxygen isotopic composition of chondrules and CAIs during high-temperature processing in the nebula (Figure 13). As such, the oxygen isotopic composition of a meteorite appears to trace the formation distance of its

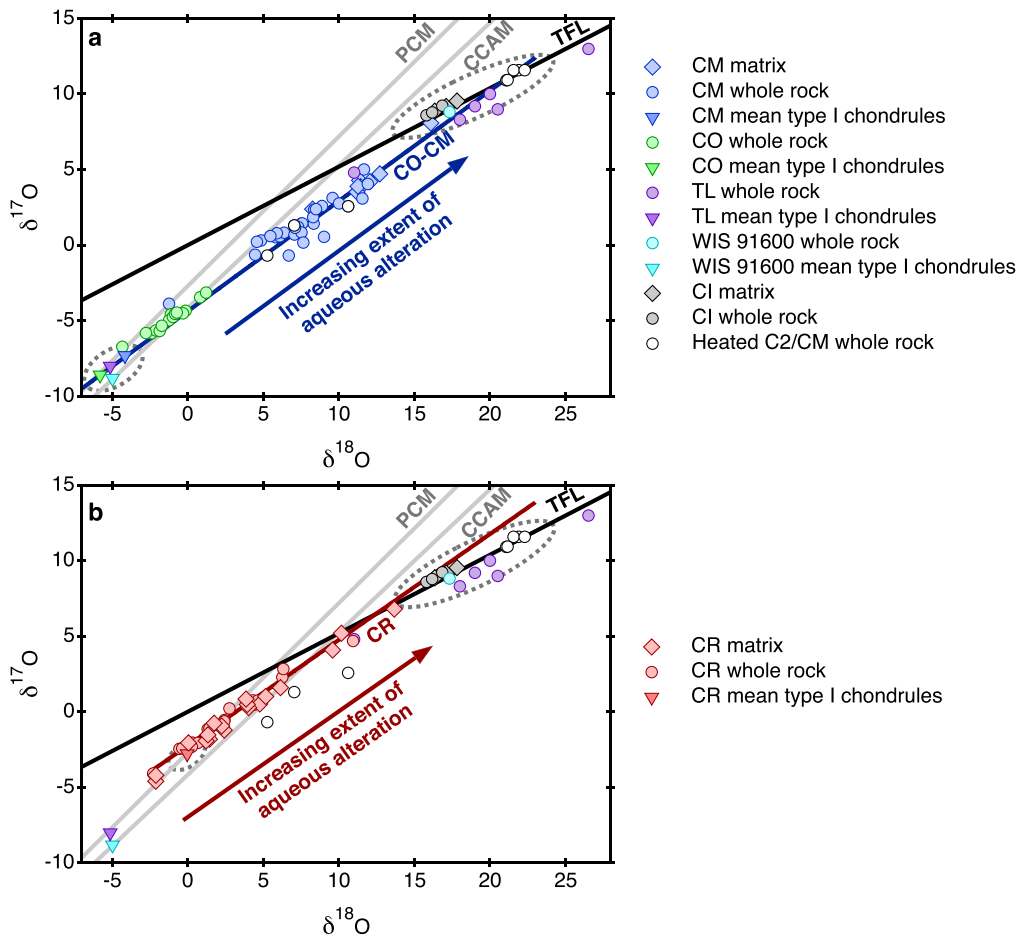


**Figure 13.** The measured oxygen isotopic compositions of a variety of bulk chondrites and their components. (a) Bulk, matrix, and type I chondrule oxygen isotopic compositions in CM chondrites, CO chondrites, CI chondrites, impact-heated CM and C2 chondrites, Tagish Lake (TL), and WIS 91600 (Rowe et al. 1994; Clayton & Mayeda 1999; Brown et al. 2000; Choe et al. 2010; Russell et al. 2010; Herd et al. 2012; Tenner et al. 2013; Tonui et al. 2014; Chaumard et al. 2018; Yamanobe et al. 2018). The oxygen isotopic signatures of a local solar system reservoir (type I chondrules) and a proposed distal solar system reservoir (WIS 91600, Tagish Lake, CI chondrites) are marked by dotted ellipses. The CO-CM trend is shown by the blue line. The primitive chondritic mineral (PCM) and carbonaceous chondrite anhydrous mineral (CCAM) lines are shown by the gray lines, and the terrestrial fractionation line (TFL) is shown by the black line. The extent of aqueous alteration in bulk and matrix samples is shown by the arrow. (b) Bulk, matrix, and type I chondrule oxygen isotopic compositions in bulk, matrix, and type I chondrules in CR chondrites (Schrader et al. 2011, 2014; Tenner et al. 2015). The CR trend is marked by the red line. The local reservoir in this mixing trend (type I chondrules in the CR chondrites) is different to that in (a), and is marked by a dotted ellipse.

components, with material that potentially formed at  $\gtrsim 10$  au displaying larger values of  $\delta^{17}\text{O}$  and  $\delta^{18}\text{O}$  relative to material that formed around the present-day heliocentric distance of the asteroid belt.

The oxygen isotopic compositions of bulk CM and CO chondrites fall on a line with slope  $\sim 0.7$  on the triple oxygen isotope diagram (Clayton & Mayeda 1999; Figure 13(a)). The oxygen isotopic compositions of the CM matrix lie on this line at the  $^{18}\text{O}$ - and  $^{17}\text{O}$ -rich end of the range of bulk compositions of this group ( $\delta^{18}\text{O} \approx 12\text{‰}$  and  $\delta^{17}\text{O} \approx 4\text{‰}$ ; Clayton & Mayeda 1999). The average oxygen isotopic compositions of type I chondrules in the CM and CO chondrites also lie on this line at  $^{18}\text{O}$ - and  $^{17}\text{O}$ -poor values ( $\delta^{18}\text{O} \approx -5\text{‰}$  and  $\delta^{17}\text{O} \approx -8\text{‰}$ ; Tenner et al. 2013; Chaumard et al. 2018). The oxygen isotopic composition of bulk CM chondrites can, therefore, be expressed as a mixture of chondrules and matrix in this group, with matrix proportions ranging from 25 to 100 vol% and an average value of 75 vol%. This average abundance matches that observed in petrographic observations of this group (Scott & Krot 2014). The most  $^{18}\text{O}$ - and  $^{17}\text{O}$ -rich material that falls close to or on this CO-CM line is the matrix of WIS 91600,

Tagish Lake, the CI chondrites, and heated CI-like (CY) chondrites (King et al. 2019). The matrix of the CM and CO chondrites can, therefore, be expressed as a mixture of distal (matrix of WIS 91600, Tagish Lake, CI chondrites, and CI-like chondrites) and local (type I chondrules from CO and CM chondrites) solar system material. Prior to parent body alteration, the matrix of a chondrite is composed of primitive micrometer-scale material inherited from the solar nebula. As such, this mixing trend argues that the micrometer-scale material in the reservoir from which the CM chondrites formed can be expressed as a mixture of local and distal material, with the proportions of distal O-bearing material in this component ranging from 60 to 95 vol% with an average value of 75 vol% in this model. This mixing trend suggests that distal micrometer-scale material traveled into the accretion reservoir of the CM and CO parent bodies ( $\sim 3.75$  au; Desch et al. 2018) by the accretion ages of the parent bodies of these chondrites ( $\sim 2.5$ – $3.5$  Myr after CAI formation; Kruahashi et al. 2008; Fujiya et al. 2012; Doyle et al. 2015). We are currently unable to constrain the distance over which this material traveled



because our observations do not constrain the heliocentric distance of the innermost extent of this distal reservoir.

A similar mixing trend also exists in the bulk and matrix oxygen isotopic composition of the CR chondrites (Schrader et al. 2011, 2014). The isotopic compositions of these meteorites also fall on a line with a slope of  $\sim 0.7$  that extends from the oxygen isotopic composition of type I chondrules in this group ( $\delta^{18}\text{O} \approx 0\text{‰}$  and  $\delta^{17}\text{O} \approx -3\text{‰}$ ; Tenner et al. 2015) to close to bulk WIS 91600, Tagish Lake, CI chondrites, and heated CI-like chondrites (Figure 13(b)). This observation indicates that the matrix of the CR chondrites can also be expressed as a mixture of local and distal micrometer-scale material, further supporting the inward migration of this micrometer-scale material in the solar system.

The CO, CM, and CR chondrites display varying degrees of aqueous alteration, with the CO chondrites being the least aqueously altered of these groups (displaying minimal aqueous alteration; Alexander et al. 2018), followed by the CR chondrites (which display a range of alteration extents; Schrader et al. 2011, 2014; Harju et al. 2014), and finally the CM chondrites (which are the most extensively aqueously altered of these groups; Rubin et al. 2007; Howard et al. 2015). The oxygen isotopic composition of more aqueously altered CO, CM, and CR material is more  $^{18}\text{O}$ - and  $^{17}\text{O}$ -rich (i.e., further along to the mixing lines toward the distal meteorites) both within and between these three groups (Rubin et al. 2007; Schrader et al. 2014; Figure 13). This observation argues that the oxygen isotopic composition of these meteorites evolves toward that of the proposed distal meteorites as they incorporated more water. This trend indicates that the ice that was accreted into the CO, CM, and CR chondrite parent bodies originates from the distal reservoir from which the WIS 91600, Tagish Lake, CI chondrite, and CI-like chondrite parent bodies accreted. This result argues that at least part of the micrometer-scale material that inwardly migrated from the far reaches of the solar system into the accretion reservoir of the CO, CM, and CR chondrites was ice. Given that the CO and CM chondrite parent bodies are predicted to have formed at very similar heliocentric distances ( $\sim 3.75$  au; Schrader & Davidson 2017; Desch et al. 2018), the extents of aqueous alteration in these groups possibly indicate that a relatively low concentration of ice had migrated to this heliocentric distance by the accretion age of the CO chondrite parent body ( $\sim 2.5$ – $3.0$  Myr after CAI formation; Doyle et al. 2015) and that this concentration had increased by the accretion age of the CM chondrite parent body ( $\sim 3.0$ – $3.5$  Myr after CAI formation; Fujiya et al. 2012). This trend, therefore, possibly tracks the inward migration of ice through a specific heliocentric distance in the solar nebula. Together, these observations propose a distal origin for the water accreted into bodies that likely formed just outside the orbit of Jupiter (Kruijer et al. 2017) as well as constraints on the timescale of its inward delivery.

A notable exception to this trend is the CM1 and CM1/2 chondrites (the most aqueously altered CM chondrites), which often display similar oxygen isotopic compositions to CM2 chondrites despite their high degree of aqueous alteration (King et al. 2017). It is possible that these meteorites were aqueously altered to such a high extent that oxygen from the minerals in their chondrules was mixed with oxygen from their matrix to create an average oxygen isotopic composition across the whole meteorite. Assuming the oxygen isotopic composition of chondrules from the CM1 and CM1/2 chondrites is similar to that from the CM2 chondrites, this process would have caused the oxygen isotopic composition of the matrix of these

meteorites to move toward  $^{18}\text{O}$ - and  $^{17}\text{O}$ -poor values, possibly explaining the relatively low  $\delta^{18}\text{O}$  and  $\delta^{17}\text{O}$  of the CM1 and CM1/2 chondrites.

## 5. Conclusions

1. The migrations of solid objects throughout the early solar system are thought to have played central roles in planet formation and disk evolution. However, our understanding of these migrations is limited by the lack of meteorite observations that provide quantitative constraints on the timing, distances, and directions involved in these processes.
2. Our solar nebula supported a magnetic field that likely decreased in intensity with distance from the Sun. The intensity of the magnetic field experienced by a meteorite that recorded its magnetic remanence within the lifetime of the disk could, therefore, be used to recover an estimate of the formation distance of its parent body. We measured the magnetic remanence carried by the WIS 91600 ungrouped C2 chondrite, finding that it experienced an ancient field intensity of  $4.4 \pm 2.8 \mu\text{T}$ . Due to the thermal history of this meteorite, this paleointensity estimate is more reliable than those recovered from previous measurements of the CM chondrites and Tagish Lake. Constrained MHD models of our nebula argue that the magnetic field it supported reached this intensity at a heliocentric distance of  $\sim 9.8$  au, indicating that the WIS 91600 parent body formed in the far reaches of the solar system. As such, our results support previous claims (Fujiya et al. 2019; Bryson et al. 2020) that the parent asteroids of some meteorites formed in this region of the solar system.
3. WIS 91600 likely came to Earth from the asteroid belt. Combined with our recovered formation distance, this observation indicates that the WIS 91600 parent body previously traveled from  $\sim 10$  au to  $\sim 2$ – $3$  au. This observation supports the scattering of asteroid-sized bodies throughout the solar system and suggests that the giant planets played a key role in establishing the large-scale architecture of the present-day solar system and the generation of the asteroid belt.
4. WIS 91600 contains chondrules, CAIs, and AOs. These millimeter-sized solids were formed by thermal processing at  $\lesssim 4$  au within  $\sim 3.5$  Myr of CAI formation. Their presence in this meteorite indicates that the earliest solids that formed in our solar system were capable of traveling outwards over large distances within just a few million years of their formation.
5. The oxygen isotopic compositions of proposed distal meteorites (WIS 91600, Tagish Lake, CI chondrites, and heated CI-like chondrites) are distinct from those of most other meteorites, suggesting that the oxygen isotopic composition of the components of a chondrite reflects their formation distances within the solar nebula. Moreover, the oxygen isotopic composition of the matrix of the CO, CM, and CR chondrites can be expressed as a mixture of local (type I chondrules) and distal material, arguing that micrometer-scale material that originated in the distal reservoir had migrated to the formation distances of the parent bodies of these chondrites by  $\sim 2.5$ – $3.0$  Myr after CAI formation. The extents of aqueous alteration in these chondrite groups argue that

at least part of the inwardly migrating micrometer-scale material was ice, proposing a distal origin for the water found in carbonaceous chondrites.

J.F.J.B. acknowledges St. John's College, University of Cambridge for funding. J.F.J.B. and B.P.W. thank the NASA Emerging Worlds program (grant #NNX15AH72G) and Thomas F. Peterson, Jr. for support. We also thank an anonymous reviewer for constructive comments that improved the quality of this manuscript. We would like to thank R. Harrison for assistance in interpreting the FORC diagrams. US Antarctic meteorite samples are recovered by the Antarctic Search for Meteorites (ANSMET) program, which has been funded by NSF and NASA, and characterized and curated by the Department of Mineral Sciences of the Smithsonian Institution and Astromaterials Curation Office at NASA Johnson Space Center. The paleomagnetic data presented in this paper can be found on the MagIC database (<https://www2.earthref.org/MagIC>).

### ORCID iDs

James F. J. Bryson  <https://orcid.org/0000-0002-5675-8545>

John B. Biersteker  <https://orcid.org/0000-0001-5243-241X>

### References

- Alexander, C. M. O. 2005, in ASP Conf. Ser. 341, Chondrites and the Protoplanetary Disk, ed. A. N. Krot, E. R. D. Scott, & B. Reipurth (San Francisco, CA: ASP), 972
- Alexander, C. M. O., Greenwood, R. C., Bowden, R., et al. 2018, *GeCoA*, 221, 406
- Bai, X. N. 2015, *ApJ*, 798, 84
- Bai, X. N., & Goodman, J. 2009, *ApJ*, 701, 737
- Beck, P., Garenne, A., Quirico, E., et al. 2014a, *Icar*, 229, 263
- Beck, P., Quirico, E., Garenne, A., et al. 2014b, *M&PS*, 49, 2064
- Biersteker, J. B., Weiss, B. P., Heinisch, P., et al. 2019, *ApJ*, 875, 39
- Birjukov, V. V., & Ulyanov, A. A. 1996, in Proc. NIPR Symp. 9, Twentieth Symposium on Antarctic Meteorites, ed. H. Kojima et al. (Tokyo: National Institute of Polar Research), 8
- Bland, P. A., Collins, G. S., Davison, T. M., et al. 2014, *NatCo*, 5, 5451
- Bland, P. A., Zolensky, M. E., Benedix, G. K., & Sephton, M. A. 2006, in Meteorites and the Early Solar System II, ed. D. S. Lauretta & H. Y. McSween, Jr. (Tucson, AZ: Univ. Arizona Press), 853
- Bonal, L., Quirico, E., Flandinet, L., & Montagnac, G. 2016, *GeCoA*, 189, 312
- Braukmuller, N., Wombacher, F., Hezel, D. C., Escoube, R., & Munker, C. 2018, *GeCoA*, 239, 17
- Briani, G., Quirico, E., Gounelle, M., et al. 2013, *GeCoA*, 122, 267
- Brown, P. G., Hildebrand, A. R., Zolensky, M. E., et al. 2000, *Sci*, 290, 320
- Brownlee, D., Tsou, P., Al on, J., et al. 2006, *Sci*, 314, 1711
- Bryson, J. F. J., Neufeld, J. A., & Nimmo, F. 2019a, *E&PSL*, 521, 68
- Bryson, J. F. J., Weiss, B. P., Abrahams, J. N. H., Nimmo, F., & Scholl, A. 2019b, *JGRE*, 124, 1880
- Bryson, J. F. J., Weiss, B. P., Harrison, R. J., Herrero-Albillos, J., & Kronast, F. 2017, *E&PSL*, 472, 152
- Bryson, J. F. J., Weiss, B. P., Lima, E. A., Gattacceca, J., & Cassata, W. 2020, *ApJ*, 892, 126
- Carporzen, L., Weiss, B. P., Elkins-Tanton, L. T., et al. 2011, *PNAS*, 108, 6386
- Chan, Q. H. S., Bodnar, M. E. Z. R. J., Farley, C., & Cheung, J. C. G. 2017, *GeCoA*, 201, 392
- Chaumard, N., Defouilloy, C., & Kita, N. T. 2018, *GeCoA*, 228, 220
- Choe, W. H., Huber, H., Rubin, A. E., Kallemeyn, G. W., & Wasson, J. T. 2010, *M&PS*, 45, 531
- Ciesla, F. 2007, *Sci*, 318, 613
- Clayton, R. N. 2003, *AREPS*, 21, 115
- Clayton, R. N., & Mayeda, T. K. 1999, *GeCoA*, 63, 2089
- Cloutis, E. A., Hudon, P., Hiroi, T., & Gaffey, M. J. 2012, *Icar*, 220, 586
- Cournede, C., Gattacceca, J., Gounelle, M., et al. 2015, *E&PSL*, 410, 62
- Cournede, C., Gattacceca, J., Rochette, P., & Shuster, D. L. 2020, *E&PSL*, 533, 116042
- Crawford, D. A., & Schultz, P. H. 1999, *IJE*, 23, 169
- Crawford, D. A., & Schultz, P. H. 2000, *LPSC*, 31, 1849
- Cuzzi, J. N., Davis, S. S., & Dobrovolskis, A. R. 2003, *Icar*, 166, 385
- Dekkers, M. J. 1988, *PEPI*, 52, 376
- DeMeo, F. E., & Carry, B. 2014, *Natur*, 505, 629
- Desch, S. J., Kalyaan, A., & Alexander, C. M. O. 2018, *ApJS*, 238, 11
- Doyle, P. M., Jogo, K., Nagashima, K., et al. 2015, *NatCo*, 6, 7444
- Egli, R. 2013, *GPC*, 110, 302
- Elkins-Tanton, L. T., Weiss, B. P., & Zuber, M. T. 2011, *E&PSL*, 305, 1
- Evans, M. E., Kr asa, D., Williams, W., & Winkhofer, M. 2006, *JGRB*, 111, B12S16
- Forman, L. V., Bland, P. A., Timms, N. E., et al. 2017, *Geo*, 45, 559
- Fu, R. R., Kehayias, P., Weiss, B. P., et al. 2020, *JGRE*, 125, e06260
- Fu, R. R., Weiss, B. P., Lima, E. A., et al. 2014, *Sci*, 346, 1089
- Fu, R. R., Weiss, B. P., Shuster, D. L., et al. 2012, *Sci*, 338, 238
- Fujiya, W., Hoppe, P., Ushikubo, T., et al. 2019, *NatAs*, 3, 910
- Fujiya, W., Sugiura, N., Hotta, H., Ichimura, K., & Sano, Y. 2012, *NatCo*, 3, 627
- Fujiya, W., Sugiura, N., Marrocchi, Y., et al. 2015, *GeCoA*, 161, 101
- Fujiya, W., Sugiura, N., Sano, Y., & Hiyagon, H. 2013, *E&PSL*, 362, 130
- Garenne, A., Beck, P., Montes-Hernandez, G., et al. 2014, *GeCoA*, 137, 93
- Gattacceca, J., & Rochette, P. 2004, *E&PSL*, 227, 377
- Gattacceca, J., Rochette, P., Denise, M., Consolmagno, G., & Folco, L. 2005, *E&PSL*, 234, 351
- Gattacceca, J., Weiss, B. P., & Gounelle, M. 2016, *E&PSL*, 455, 166
- Gomes, R., Levison, H. F., Tsiganis, K., & Morbidelli, A. 2005, *Natur*, 435, 466
- Grady, M. M., Verchovsky, A. B., Franchi, I. A., Wright, I. P., & Pillinger, C. T. 2002, *M&PS*, 37, 713
- Granvik, M., & Brown, P. 2018, *Icar*, 311, 271
- Greenwood, R. C., Franchi, I. A., Kearsley, A. T., & Alard, O. 2010, *GeCoA*, 74, 1684
- Hanna, R. D., Ketcham, R. A., Zolensky, M., & Behr, W. M. 2015, *GeCoA*, 171, 256
- Harju, E. R., Rubin, A. E., Ahn, I., et al. 2014, *GeCoA*, 139, 267
- Harrison, R. J., & Feinberg, J. M. 2008, *GGG*, 9, Q05016
- Harrison, R. J., & Lascu, I. 2014, *GGG*, 15, 4671
- Harrison, R. J., Murszko, J., Heslop, D., et al. 2018, *GGG*, 19, 1595
- Hartmann, L., Calvert, N., Gullbring, E., & D'Alessio, P. 1998, *ApJ*, 495, 385
- Herd, C. D. K., Sharp, Z. D., Alexander, C. M. O., & Blinova, A. 2012, *LPSC*, 43, 1688
- Hiroi, T., Tonui, E., Pieters, C. M., et al. 2005, *LPSC*, 36, 1564
- Hiroi, T., Zolensky, M. E., & Pieters, C. M. 2001, *Sci*, 293, 2234
- Howard, K. T., Alexander, C. M. O., Scharder, D. L., & Dyl, K. A. 2015, *GeCoA*, 149, 206
- Jenniskens, P., Fries, M. D., Yin, Q.-Z., et al. 2012, *Sci*, 338, 1583
- Jilly, C. E., Huss, G. R., Krot, A. N., et al. 2014, *M&PS*, 49, 2104
- Jilly-Rehak, C. E., Huss, G. R., & Nagashima, K. 2017, *GeCoA*, 201, 224
- Joswiak, D. J., Brownlee, D. E., Nguyen, A. N., & Messenger, S. 2017, *M&PS*, 52, 1612
- Kelly, D. P., & Vaughan, D. J. 1983, *MinM*, 47, 453
- Kimura, M., Grossman, J. N., & Wiesberg, M. K. 2011, *M&PS*, 46, 431
- Kimura, Y., Sato, T., Nakamura, N., et al. 2013, *NatCo*, 4, 2649
- King, A. J., Bates, H. C., Krietsch, D., et al. 2019, *Geoch*, 79, 125531
- King, A. J., Schofield, P. F., Howard, K. T., & Russell, S. S. 2015, *GeCoA*, 165, 148
- King, A. J., Schofield, P. F., & Russell, S. S. 2017, *M&PS*, 52, 1197
- Kirschvink, J. L., Kopp, R. E., Raub, T. D., Baumgartner, C. T., & Holt, J. W. 2008, *GGG*, 9, Q05Y01
- Kletetschka, G., & Wiczorek, M. A. 2017, *PEPI*, 272, 44
- Krot, A. N., Hutcheon, I. D., Brearley, A. J., et al. 2006, in Meteorites and the Early Solar System II, ed. D. S. Lauretta & H. Y. McSween, Jr. (Tucson, AZ: Univ. Arizona Press)
- Kruahashi, E., Kita, N. T., Nagahara, H., & Morishita, Y. 2008, *GeCoA*, 72, 3865
- Kruijjer, T. S., Burkhardt, C., Budde, G., & Kleine, T. 2017, *PNAS*, 114, 6712
- Kruijjer, T. S., Kleine, T., & Borg, L. E. 2019, *NatAs*, 2, 32
- Lee, M. R., Lindgren, P., & Sofe, M. R. 2014, *GeCoA*, 144, 126
- Levison, H. F., Bottke, W. F., Gounelle, M., et al. 2009, *Natur*, 460, 364
- Lichtenberg, T., Golabek, G. J., Dullemond, C. P., et al. 2018, *Icar*, 302, 27
- Lindgren, P., Hanna, R. D., Dobson, K. J., Tomkinson, T., & Lee, M. R. 2015, *GeCoA*, 148, 159
- McClelland, E. 1996, *GeoJI*, 126, 271
- Moriarty, G. M., Rumble, D., & Friedrich, J. M. 2009, *ChEG*, 69, 161
- Morris, M. A., Garvie, L. A. J., & Knauth, L. P. 2015, *ApJL*, 801, L22
- Muxworthy, A. R., Bland, P. A., Davison, T. M., et al. 2017, *M&PS*, 52, 2132

- Muxworthy, A. R., & Dunlop, D. J. 2002, *E&PSL*, **203**, 369
- Nagy, L., Williams, W., Muxworthy, A. R., et al. 2017, *PNAS*, **114**, 10356
- Nakamura, T. 2005, *JMPeS*, **100**, 260
- Nesvorny, D. 2018, *ARA&A*, **56**, 137
- Opeil, C. P., Consolmagno, G. J., Safarik, D. J., & Britt, D. T. 2012, *M&PS*, **47**, 319
- Oran, R., Weiss, B. P., & Cohen, O. 2018, *E&PSL*, **492**, 222
- Paterson, G. A. 2011, *JGR*, **116**, B10104
- Paterson, G. A., Tauxe, L., Biggin, A. J., Shaar, R., & Jonestrask, L. C. 2014, *GGG*, **15**, 1180
- Pravdivtseva, O., Krot, A. N., & Hohenberg, C. M. 2018, *GeCoA*, **227**, 38
- Quirico, E., Bonal, L., Beck, P., et al. 2018, *GeCoA*, **241**, 17
- Raymond, S. N., & Izidoro, A. 2017, *SciA*, **3**, e1701138
- Roberts, A. P., Almeida, T. P., Church, N. S., et al. 2017, *JGRB*, **122**, 9534
- Roberts, A. P., Heslop, D., Zhao, X., & Pike, C. R. 2014, *RvGeo*, **52**, 557
- Roberts, A. P., Liu, Q., Rowan, C. J., et al. 2006, *JGRB*, **111**, B12S35
- Roberts, A. P., Tauxe, L., Heslop, D., Zhao, X., & Jiang, Z. 2018, *JGRB*, **123**, 2618
- Rochette, P., Gattacceca, J., Bonal, L., et al. 2008, *M&PS*, **43**, 959
- Rowe, M. W., Clayton, R. N., & Mayeda, T. K. 1994, *GeCoA*, **58**, 5341
- Rubin, A. E. 2012, *GeCoA*, **90**, 181
- Rubin, A. E., & Harju, E. R. 2012, *M&PSA*, **75**, 5022
- Rubin, A. E., Trigo-Rodriguez, J. M., Huber, H., & Wasson, J. T. 2007, *GeCoA*, **71**, 2361
- Russell, S. D. J., Longstaffe, F. J., King, P. L., & Larson, T. E. 2010, *GeCoA*, **74**, 2484
- Schrader, D. L., & Davidson, J. 2017, *GeCoA*, **214**, 157
- Schrader, D. L., Davidson, J., Greenwood, R. C., Franchi, I. A., & Gibson, J. M. 2014, *E&PSL*, **407**, 48
- Schrader, D. L., Franchi, I. A., Connolly, H. C., et al. 2011, *GeCoA*, **75**, 308
- Schrader, D. L., Nagashima, K., Waitukaitis, S. R., et al. 2018, *GeCoA*, **223**, 405
- Scott, E. R. D. 2007, *AREPS*, **35**, 577
- Scott, E. R. D., & Krot, A. N. 2014, in *Meteorites, Comets, and Planets, Treatise on Geochemistry*, Vol. 1, ed. H. D. Holland & K. K. Turekian (Amsterdam: Elsevier), 143
- Stephenson, A. 1993, *JGR*, **98**, 373
- Tauxe, L., Gans, P., & Mankinen, E. A. 2004, *GGG*, **5**, Q06H12
- Tauxe, L., & Staudigel, H. 2004, *GGG*, **5**, Q02H06
- Tenner, T. J., Nakasima, D., Ushikubo, T., Kita, N. T., & Wiesberg, M. K. 2015, *GeCoA*, **148**, 228
- Tenner, T. J., Ushikubo, T., Kruahashi, E., Kita, N. T., & Nagahara, H. 2013, *GeCoA*, **102**, 226
- Tonui, E., Zolensky, M., Hiroi, T., et al. 2014, *GeCoA*, **126**, 284
- Ushikubo, T., Kimura, M., Kita, N. T., & Valley, J. W. 2012, *GeCoA*, **90**, 242
- Vacher, L. G., Marrocchi, Y., Villeneuve, J., Verdier-Paoletti, M. J., & Gounelle, M. 2018, *GeCoA*, **239**, 213
- Verdier-Paoletti, M. J., Marrocchi, Y., Avicé, G., et al. 2017, *E&PSL*, **458**, 273
- Walsh, K. J., Morbidelli, A., Raymond, S. N., O'Brien, D. P., & Mandell, A. M. 2011, *Natur*, **475**, 206
- Wang, H., Weiss, B. P., Bai, X.-N., et al. 2017, *Sci*, **355**, 623
- Wardle, M. 2007, *Ap&SS*, **311**, 35
- Wehland, F., Stancu, A., Rochette, P., Dekkers, M. J., & Appel, E. 2005, *PEPI*, **153**, 181
- Weiss, B. P., Gattacceca, J., Stanley, S., Rochette, P., & Christensen, U. R. 2010, *SSRv*, **152**, 341
- Weiss, B. P., & Tikoo, S. M. 2014, *Sci*, **346**, 1246753
- Yabuta, H., Alexander, C. M. O., Fogel, M. L., Kilcoyne, A. L. D., & Cody, G. D. 2010, *M&PS*, **45**, 1446
- Yamanobe, M., Nakamura, T., & Nakasima, D. 2018, *PolSc*, **15**, 29
- Zolensky, M. E., Nakamura, K., Gounelle, M., et al. 2002, *M&PS*, **37**, 737